frontiers in Marine Science

TYPE Original Research
PUBLISHED 18 February 2026
DOI 10.3389/fmars.2026.1711689



OPEN ACCESS

EDITED BY
Jun Sun,
Tianjin University of Science and Technology, China

REVIEWED BY
Jeonghyun Kim,
Jeju National University, Republic of Korea
Xilin Xiao,
Xiamen University, China
Quentin Devresse,
Helmholtz Association of German Research Centres (HZ), Germany

*CORRESPONDENCE
J. L. García
jlgarcia@iim.csic.es
X. A. Álvarez-Salgado
xsalgado@iim.csic.es

RECEIVED 23 September 2025
REVISED 27 January 2026
ACCEPTED 31 January 2026
PUBLISHED 18 February 2026

CITATION
García JL, Arístegui J, Pazó MJ, Vieitez dos Santos V, Hernández-Hernández N, Nieto-Cid M, Gelado-Caballero MD, Martínez-Marrero A and Álvarez-Salgado XA (2026) Mesoscale and submesoscale variability of organic matter in island-induced eddies across their life cycle: implications for the biological carbon pump.
*Front. Mar. Sci.* 13:1711689.
doi: 10.3389/fmars.2026.1711689



# Mesoscale and submesoscale variability of organic matter in island-induced eddies across their life cycle: implications for the biological carbon pump

J. L. García[1,2*], J. Arístegui[2], M. J. Pazó[1], V. Vieitez dos Santos[1], N. Hernández-Hernández[2], Mar Nieto-Cid[1,3], M. D. Gelado-Caballero[2], A. Martínez-Marrero[2] and X. A. Álvarez-Salgado[1*]

[1]Laboratorio de Geoquímica Orgánica, Instituto de Investigacións Mariñas (CSIC), Vigo, Spain, [2]Instituto de Oceanografía y Cambio Global, Universidad de Las Palmas de Gran Canaria, Telde, Spain, [3]Instituto Español de Oceanografía, CO A Coruña (IEO-CSIC), A Coruña, Spain

The Canary Islands region exhibits intense mesoscale activity, with eddies generated south the islands by perturbations of the Canary Current. After detachment, these eddies drift southwestward along the Canary Eddy Corridor (CEC), exporting their properties into the open ocean. While mesoscale dynamics in the region are well documented, associated submesoscale structures and their role in the production, transport and remineralization of organic matter remain poorly understood. We investigated meso- and submesoscale variability of dissolved organic carbon (DOC), suspended particulate organic carbon (POCsus), and the chromophoric (CDOM) and fluorescent (FDOM) fractions of dissolved organic matter (DOM), at high spatial resolution across four eddies sampled in 2022. In summer, we studied three newly formed or developing eddies: the cyclonic Garajonay eddy, trapped between La Gomera and El Hierro Islands and sustaining an intense phytoplankton bloom and a developing eddy pair south of Gran Canaria (cyclonic Nublo) and Tenerife (anticyclonic Anaga). In autumn, we sampled Bentayga, a five- month-old anticyclonic intrathermocline eddy drifting along the CEC. Cyclonic eddies showed decreasing DOC, CDOM and protein-like FDOM with age, whereas anticyclonic eddies accumulated humic-like FDOM. At the submesoscale, DOC decreased above the pycnocline and humic-like FDOM below it across the Nublo-Anaga front, while Bentayga exhibited pronounced intra-eddy submesoscale variability in DOC, CDOM, and humic-like FDOM. The residuals of the multiple regression with the thermohaline variables of apparent oxygen utilization (ΔAOU), ΔDOC, ΔPOC, ΔCDOM and ΔFDOM, are independent of water mass mixing and physical motions, and therefore retain the biogeochemical variability associated with local processes. Significant correlations among the residuals of DOC/AOU, CDOM/AOU and FDOM/AOU highlight the central role of DOM in local remineralization, which accounts for up to 68 ± 15% of mesopelagic oxygen demand, resulting in the accumulation of humic-like substances and substantial consumption of chromophoric and protein-like materials. Furthermore, the combined residual

relationships of DOC/AOU and POCsus/AOU indicate that up to 88% of mesopelagic oxygen demand in the CEC is driven by local remineralization of DOC and POCsus, suggesting only a minor contribution from sinking POM. Our results demonstrate that meso- and submesoscale processes strongly regulate organic matter transport, remineralization and oxygen consumption in the CEC.

KEYWORDS

Canary Eddy Corridor, chromophoric dissolved organic matter (CDOM), dissolved organic carbon (DOC), fluorescent dissolved organic matter (FDOM), subtropical northeast Atlantic Ocean, suspended particulate organic carbon (POCsus)

# 1 Introduction

Mesoscale eddies, with tens to hundreds of km in size and life spans from days to months, are ubiquitous in the global ocean, travelling from hundreds to thousands of km before they dissipate, playing a critical role in regulating primary production, food web dynamics, and biogeochemical cycles (Chelton et al., 2011; Devresse et al., 2023; McGillicuddy, 2016). These structures -cyclonic or anticyclonic (Barceló-Llull et al., 2017; Chelton et al., 2011)- may arise from current instabilities, topographic interactions, and eddy-eddy encounters (Cardoso et al., 2020; Chelton et al., 2011; McGillicuddy, 2016; Sangrà et al., 2009). A particular type of anticyclonic eddies, are the intrathermocline eddies, which are subsurface eddies rotating anticyclonically but with a dome-shaped isopycnals in the upper layers (Barceló-Llull et al., 2017; McGillicuddy et al., 2007).

Traditionally, mesoscale motions have been regarded as the primary drivers controlling the distribution of biogeochemical properties and ecosystem dynamics in the upper ocean, as they can pump nutrients into the euphotic zone (Lévy et al., 2018; Mahadevan & Tandon, 2006; McGillicuddy et al., 2007; Nagai et al., 2008). However, basin-scale estimates indicate that mesoscale processes alone cannot provide the nutrient flux required to sustain the observed productivity in certain regions of the ocean, such as the subtropical gyres (Mahadevan & Tandon, 2006). Modeling studies have also shown that density fronts can enhance vertical exchanges, underscoring the importance of smaller-scale processes, commonly referred to as submesoscale activity (Hernández-Hernández et al., 2020; Mahadevan & Tandon, 2006).

Regarding their life span, cold-core cyclonic eddies are commonly categorized into three stages: intensification or spin-up (<2 months, dominated by nutrient injection), maturity (~2–3 months, characterized by biological responses with increasing export toward the later stages), and decay or relaxation (>3 months, dominated by particle export; Maiti et al., 2008; Sweeney et al., 2003). However, a recent work by Zhu et al. (2023) showed that in a decaying cyclonic eddy, vertical particle export can be reduced due to accelerated remineralization and fragmentation within the eddy. Throughout an eddy's life span, the heterogeneity of biomass and export is shaped by the variability in three-dimensional water flow (McGillicuddy et al., 2007; Zhou et al., 2020). By contrast to cyclonic eddies, the life cycle of a Canarian anticyclonic eddy was described by Sangrà et al. (2005). Their observations indicate that the eddy transitions from an early stage, through a mature stage to a decay stage is marked by a substantial reduction of the vorticity maximum.

Submesoscale motions arise from mesoscale eddies and boundary currents, generated by instabilities, topographic wakes, and frontogenesis (Mahadevan, 2016; McWilliams, 2016). The latter appears to be particularly important, as submesoscale dynamics are often closely associated with fronts (Lévy et al., 2018). These submesoscale features typically have temporal and spatial scales of a few days and kilometers, respectively (Hernández-Hernández et al., 2020; Lévy et al., 2018; Zhang et al., 2019). Unlike mesoscale motions, submesoscale processes are not well approximated by geostrophic balance because, at these scales, Rossby and Richardson numbers approach unity in localized regions. This generates strong ageostrophic secondary circulation that acts to restore geostrophy, producing large vertical velocities that significantly influence nutrient transport (Hernández-Hernández et al., 2020; Lévy et al., 2018; Mahadevan & Tandon, 2006), which consequently affects surface chlorophyll-*a* concentrations (Chl-*a*; Maiti et al., 2008; McGillicuddy et al., 2007), phytoplankton biomass and carbon cycling (Brannigan et al., 2017; Lévy et al., 2018).

Submesoscale processes remain poorly resolved in Earth System Models, limiting the accuracy of biogeochemical forecasting in general (Bonan and Doney, 2018; McWilliams, 2008), and particularly that of the biological carbon pump (Ducklow, 2001). Accurate modeling of the biological carbon pump requires resolving both mesoscale and submesoscale processes and explicitly accounting for all particulate organic carbon (POC) pools, defined here as the sum of sinking and suspended fractions, as well as dissolved organic carbon (DOC; Boyd et al., 2019). While the vertical flux of fast (> 20 m $d^{-1}$) and slow (< 20 m $d^{-1}$; Riley et al., 2012) sinking POC is governed by gravity, the vertical fluxes of suspended POC (POCsus) and DOC depend on advective and diffusive forces. These processes are known to occur in mesoscale eddies, although their impact on the distributions of DOC and POCsus across spatial and temporal scales remain insufficiently constrained (Mahadevan, 2016).

In this study, we focus specifically on eddies generated in the Canary Archipelago, a region that serves as a natural laboratory for investigating interactions between mesoscale and submesoscale processes and their biogeochemical impacts. Recurrent cyclonic-anticyclonic eddy pairs form downstream of the islands as a result of the interplay between island topography and the Canary Current

(Arístegui et al., 1994, 1997; Cardoso et al., 2020; Sangrà et al., 2007, 2009). These eddies are primarily generated by perturbations in the mean flow, although Ekman pumping driven by wind stress may intensify their development during generation and evolution (Jiménez et al., 2008). Many of these eddies, once detached downstream of the islands, drift southwestward along the Canary Eddy Corridor (CEC), a pathway that transports biological and biogeochemical properties across the transition zone of the Canary Current Upwelling region toward the oligotrophic open-ocean waters of the North Atlantic Subtropical Gyre (Figure 1A; Arístegui et al., 1994, 1997; Barton et al., 1998; Sangrà et al., 2009). As they travel along the CEC, eddies often grow in size and intensity, enhancing regional biogeochemical connectivity (Álvarez-Salgado and Arístegui, 2015). The lifespan of these eddies can extend for more than a year, depending on the initial intensity and the eddy-eddy interactions (Sangrà et al., 2009).

Numerous studies in the region have demonstrated strong feedbacks between physical processes and biological-biogeochemical responses in mesoscale eddies, based on a combination of theory, field observation, remote sensing, and modelling approaches (e.g., Arístegui et al., 1997, 2003; Arístegui and Montero, 2005; Barton et al., 1998; Barton and Arístegui, 2004; Hernández-Hernández et al., 2020). However, the links between mesoscale and submesoscale dynamics throughout the eddy life cycle, and their influence on organic matter cycling, remain poorly understood. This knowledge gap is primarily due to the scarcity of process-oriented field studies with sufficiently high spatial resolution to resolve submesoscale processes and to validate coupled physical-biological models (Hernández-Hernández et al., 2021; Lévy et al., 2018; Mahadevan, 2016; Shi et al., 2024). The main objective of this study is to assess the role of mesoscale eddies and their associated submesoscale dynamics in the biological carbon pump by investigating how these structures influence the distribution of dissolved and suspended particulate organic matter across different eddy life stages in the Canary region.

## 2 Materials and methods

### 2.1 Sampling strategy and eddy characterization

Fieldwork was carried out during two research cruises aboard R/V Sarmiento de Gamboa: the first, eIMPACT-1 (July 29$^{th}$ to August 25$^{th}$, 2022), focused on sampling recently formed eddies,

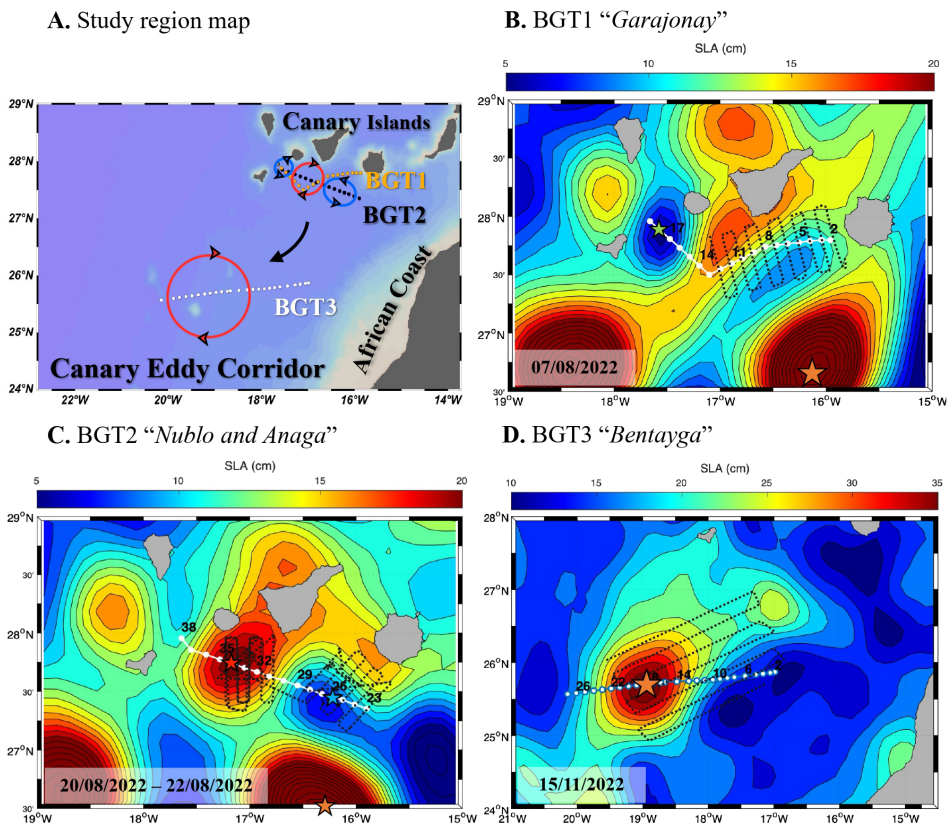


FIGURE 1
**(A)** Conceptual map of the Eastern North Atlantic Ocean, south of the Canary Islands, showing the general westward movement of eddies (black arrow) along the Canary Eddy Corridor (Sangrá et al., 2009). The three biogeocheinical transects (BGT1–3) are marked with different colored dots. Cyclonic eddies (Garajonay and Nublo) are indicated with blue circles, and anticyclonic eddies (Anaga and Bentayga) with red circles, showing their positions and rotation senses. **(B–D)** Sea Level Anomaly (SLA) maps corresponding to the sampling dates of Garajonay **(B)**, Nublo and Anaga **(C)**, and Bentayga **(D)**. The Nublo-Anaga SLA map represents an average, as both eddies were sampled along the same transect but on different days. Colored stars mark the eddy centers: green for Garajonay, blue for Nublo, red for Anaga, and orange for Bentayga. Dashed black lines show the SeaSoar-SADCP survey grids used to locate eddy centers prior to sampling.

while the second, eIMPACT-2 (November 7th to December 7th, 2022), conducted three months later, targeted a mature eddy drifting along the CEC.

Mesoscale eddies in the CEC were identified and tracked using a combination of satellite data and *in situ* measurements. Satellite-derived products included sea surface temperature and Chl-*a* from VIIRS, medium- to high-resolution Chl-*a* from Sentinel-3, sea level anomaly from AVISO, and sea surface height from Copernicus Marine Environment Monitoring Service products for the Iberian-Biscay-Ireland region and Mercator model outputs. These remote sensing data were complemented with *in situ* measurements from expendable bathythermographs (T7, Sippican), SeaSoar MKII (Chelsea Instruments) surveys down to 400 dbar, and shipboard Acoustic Doppler Current Profiler (SADCP; Ocean Surveyor, RD Instruments).

During the eIMPACT-1 cruise, a recently generated eddy pair -comprising the cyclonic eddy "Nublo" and the anticyclonic eddy "Anaga", located southwest of Gran Canaria and Tenerife, respectively- as well as an already developed cyclonic eddy, "Garajonay", situated between La Gomera and El Hierro, were examined (Figure 1A). Garajonay was first detected by remote sensing (sea surface temperature and sea level anomaly) one month before it was sampled on 7 August and persisted for nearly a month, after which no surface signal was observed. The Nublo-Anaga eddy pair began forming in late July, just prior to the start of the cruise. These eddies remained attached to the islands throughout the cruise and until mid-September, when they apparently merged and dissipated (Supplementary Figure S1).

Two biogeochemical transects (BGTs) were conducted during this cruise, each consisting of CTD-rosette stations (Stns) spaced every 5–6 nautical miles. BGT1 (Stns 1-19) crossed the center of Garajonay, located at Stn 18 (27.88°N-17.56°W; Figure 1B). The centers of the Nublo-Anaga eddy pair were surveyed during BGT2 (Stns 23-38; Figure 1C). Nublo extended from Stns 24 to 29 (Supplementary Figure S2A) with its center at Stn 26 (27.45°N-16.22°W; Figure 1C). Anaga expanded Stns 32 to 37 (Supplementary Figure S2A), with altimetry suggesting its center at station 34 (Figure 1C). However, SADCP data indicated that the actual center was at Stn 33 (Supplementary Figure S2A), located at 27.70°N, 17.05°W (Figure 1C). Stns 29, 30 and 31 were located at the frontal zone between Nublo and Anaga.

By the time of the eIMPACT-2 cruise, the eddies Garajonay, Nublo and Anaga had either dissipated or merged with other structures. During this cruise, we studied a large, mature intrathermocline anticyclonic eddy, named "Bentayga", centered at 25.7°N, 19.0°W, drifting along the CEC (Figure 1A). Bentayga was generated south of Gran Canaria around mid-June 2022, approximately five months before it was sampled during the cruise (Supplementary Figure S1 and Figures 1–3 in Valencia et al., 2025), and had already been observed developing south of Gran Canaria Island during the eIMPACT1 cruise (Figures 1B, C). The eddy was sampled along BGT3 (Stns 2-27; Figure 1D). According to Cerdán-García et al. (2024), the current velocity perpendicular to the transect (azimuthal velocity) obtained with the SADCP at 50 m revealed a three-zone structure (Supplementary Figure S2B); The core (stations 15-20) exhibited anticyclonic, near-solid-body rotation. The inner ring (stations 13–15 in the eastern sector and 20–23 in the western sector) exhibited negative relative vorticity but not rigid rotation. The outer ring (stations 12–13 and 23-26) exhibited positive relative vorticity.

Seawater was sampled using a CTD-rosette (Seabird 911 Plus) equipped with a dissolved oxygen sensor (SBE43), a chlorophyll-fluorescence sensor (SeaPoint SCF) and a PAR/irradiance sensor (Biospherical/LICOR Chelsea). Salinity was calculated from conductivity measurements using the TEOS 10 algorithms (IOC, SCOR and IAPSO, 2010), and was calibrated with discrete measurements performed with a Guildline 8410-A Portasal salinometer. Likewise, data from the oxygen sensor was adjusted with Winkler potentiometric analysis (described below). The chlorophyll fluorescence sensor was factory-calibrated, so fluorescence was used as a proxy for Chl-*a* (hereafter referred to as FChl-*a*).

Discrete water samples were collected from 12 depths (surface to 1500 dbar) with 12 L Niskin bottles. At stations with high water sampling demand, two CTD casts were performed: one for the epipelagic layer (5–200 dbar), focusing on the surface mixed layer, the pycnocline and the deep chlorophyll maximum (DCM); and another cast for the mesopelagic layer (200–1500 dbar).

The pycnocline was defined as the depth corresponding to the maximum Brünt-Väisälä frequency ($N^2$), calculated using the equation (Millard et al., 1990):

$$N^2 = \frac{-g}{\rho} * \frac{d(\rho)}{d(z)}$$

where g is the acceleration of gravity (9.81 m $s^{-2}$) and ρ is the potential density (Fofonoff and Millard, 1983).

## 2.2 Chemical and biological analyses

### 2.2.1 Dissolved oxygen, nutrient salts and organic carbon/nitrogen measurements

Dissolved oxygen (DO) was determined using the Winkler (1888) method with potentiometric endpoint detection (Langdon, 2010). Apparent oxygen utilization (AOU) was calculated as the difference between DO saturation and measured DO as following Benson and Krause (1984). The associated measurement error of AOU was approximately 1 μmol $kg^{-1}$. Seawater samples for the determination of ammonium ($NH_4^+$), nitrite ($NO_2^-$), nitrate ($NO_3^-$), phosphate ($PO_4^{3-}$) and silicate ($SiO_4^{4-}$) were collected directly from the Niskin bottles in 25 mL pre-cleaned polyethylene bottles and stored at -20°C until analysis at the base laboratory. They were determined by segmented flow analysis with colorimetric detection (Hansen and Koroleff, 1999), except ammonium that was determined using the fluorometric method (Kérouel and Aminot, 1997). The measurement errors were as follows: $NH_4^+$, 0.05 μmol $L^{-1}$; $NO_2^-$, 0.01 μmol $L^{-1}$; $NO_3^-$, 0.05 μmol $L^{-1}$; $PO_4^{3-}$, 0.01 μmol $L^{-1}$; and $SiO_4^{4-}$, 0.05 μmol $L^{-1}$. Dissolved inorganic nitrogen (DIN) was calculated as the sum of $NH_4^+$, $NO_2^-$ and $NO_3^-$.

Dissolved organic carbon (DOC) samples were collected from Niskin bottles into pre-combusted (450°C, 12h) 25 mL amber glass flasks and stored frozen (−20°C). DOC concentrations were

10.3389/fmars.2026.1711689

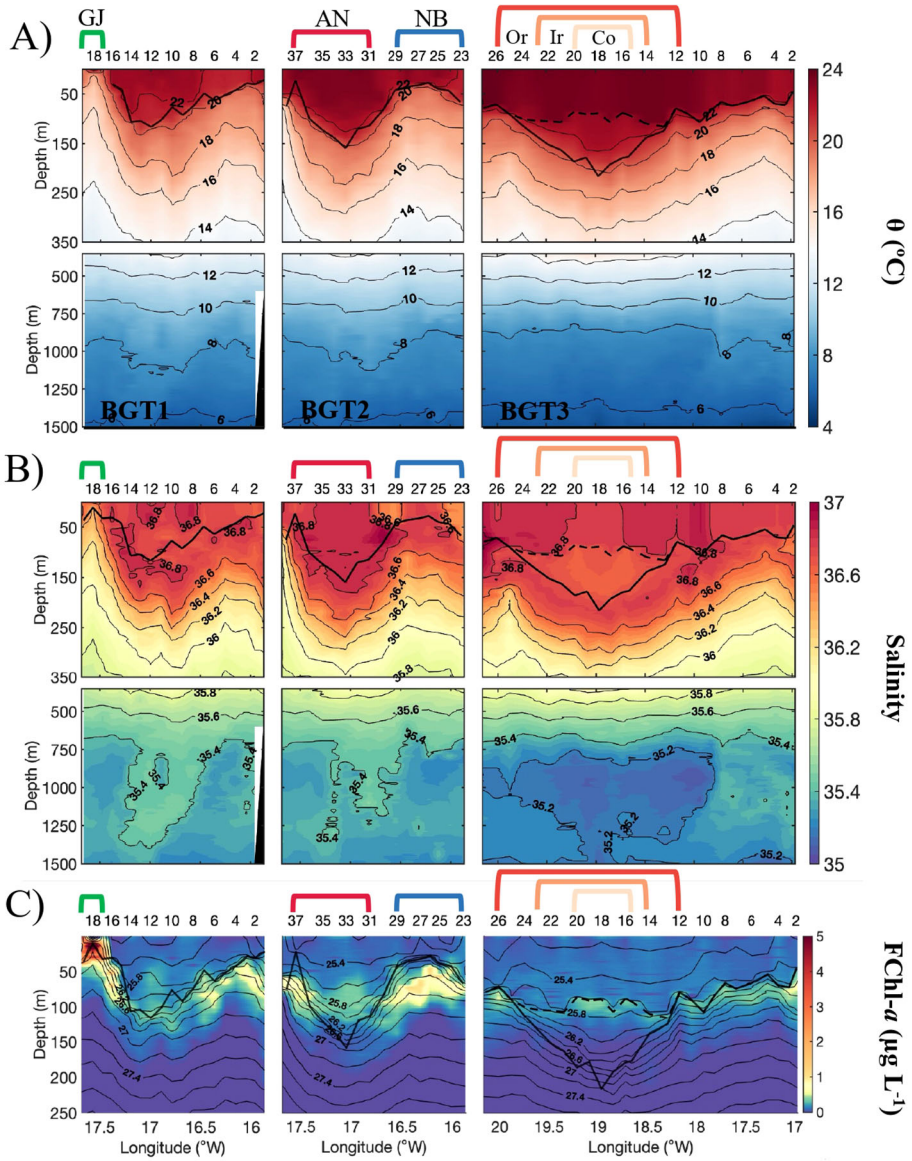


FIGURE 2
Vertical distributions of **(A)** potential temperature (θ, °C), **(B)** salinity (S) and **(C)** chlorophyll-*a* fluorescence (FChl-*a*, µg $L^{-1}$), with isopycnals superimposed. Vertical resolution of 1 dbar. Each box, along the horizontal axis, represents one of the biogeochemical transects (BGT1, BGT2, BGT3; left to right). Colored brackets indicate the presence of eddies–Garajonay (GJ; green), Anaga (AN; red), Nublo (NB; blue), and Bentayga (orange tones). For Bentayga, the core (Co), inner ring (Ir) and outer ring (Or) are distinguished. Pycnoclines are shown as thick black lines; in Bentayga, a dashed line marks the upper pycnocline and the boundary of the low-salinity core.

determined by high-temperature catalytic oxidation (680°C) using a Shimadzu TOC-V analyzer. The measurement error was 1-2 µmol $L^{-1}$. Consensus reference materials provided by Hansell's CRM Program (University of Miami, USA) were used to check the instrument performance. Our concentrations for the deep-sea water reference (Batch 16 Lot # 05-16) were 44.6 ± 1.7 µmol $L^{-1}$ (n = 14) while the certified value is 43-45 µmol $L^{-1}$. Samples for suspended particulate organic carbon (POCsus) and nitrogen (PONsus) were collected in polyethylene containers, using volumes from 2 L for surface samples to 5 L for deeper ones, which were filtered through pre-combusted (450°C, 4 h) GF/F filters (< 300 mm Hg pressure), dried for 12 h in a vacuum desiccator with silica gel, and frozen (−20°C) until analysis. Determinations were conducted using high-temperature combustion (900°C) in a Perkin Elmer 2400 elemental analyzer. The measurement error was 0.2-0.4 µmol $L^{-1}$ for POCsus and 0.02-0.04 µmol $L^{-1}$ for PONsus.

A number of unusually high POCsus values were observed along BGT3 (Supplementary Figure S3A). These elevated concentrations are interpreted as carbon-rich particles likely originating from the wildfires that affected the Island of Tenerife during summer 2022, representing an external allochthonous input rather than eddy-driven variability. Because this external influence alters the local POCsus-PON relationship, POCsus data from BGT3 were excluded from the statistical analyses. To overcome the resulting data limitation and provide a consistent framework, POCsus concentrations along BGT3 were recalculated using an orthogonal distance regression between PONsus and non-anomalous POCsus measurements from BGT3, together with all

10.3389/fmars.2026.1711689

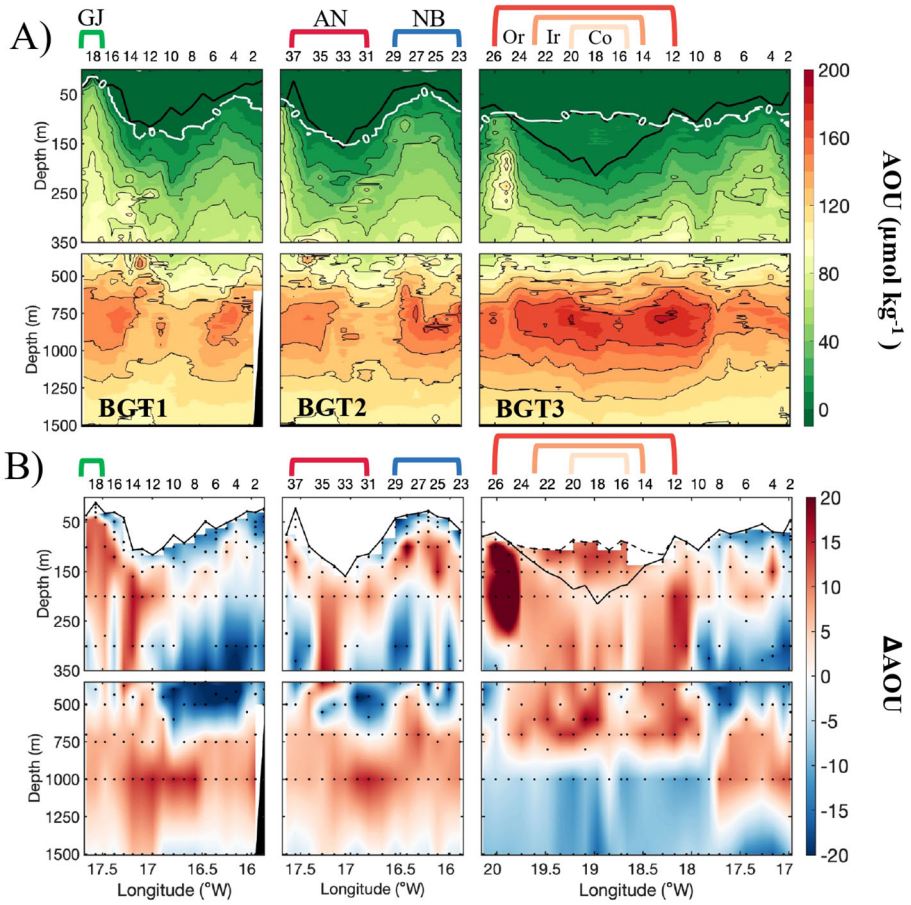


FIGURE 3
Vertical distributions of **(A)** apparent oxygen utilization (AOU), in µmol kg$^{-1}$. Vertical resolution of 1 dbar. Zero µmol kg$^{-1}$ isoline is marked by the white line; and **(B)** its corresponding residuals (△AOU). Each box, along the horizontal axis, represents one of the biogeochemical transects (BGT1, BGT2, BGT3; left to right). Colored brackets indicate the presence of eddies–Garajonay (GJ; green), Anaga (AN; red), Nublo (NB; blue), and Bentayga (orange tones). For Bentayga, the core (Co), inner ring (Ir) and outer ring (Or) are distinguished. Pycnoclines are shown as thick black lines; in Bentayga, a dashed line marks the upper pycnocline and the boundary of the low-salinity core.

POCsus data from BGT1 and BGT2 (Supplementary Figures S3B, C). The resulting orthogonal distance regression was: POCsus = 7.30 (± 0.12) × PONsus + 0.16 (± 0.05), $R^2 = 0.87$, n= 505; $p = 4.46 \times 10^{-229}$.

## 2.2.2 Absorption and fluorescence spectroscopy of dissolved organic matter

Samples for the on-board determination of chromophoric (CDOM) and fluorescent (FDOM) dissolved organic matter were collected in acid-clean 250 mL glass flasks, stored in the dark during 1–2 h to equilibrate to lab temperature, and filtered through pre-combusted (450°C, 4 h) GF/F filters using an all-glass, acid-clean, system under high-purity nitrogen pressure. Filtrates were directly transferred to both spectrophotometer and spectrofluorometer cuvettes.

CDOM absorption spectra (250-700 nm) were recorded with a Jasco V-750 double-beam spectrophotometer using 10 cm quartz cells and 0.5 nm bandwidth. Milli-Q water served as the direct reference blank. Absorption coefficients, $a_{CDOM}(\lambda)$, were calculated as:

$$a_{CDOM}(\lambda) = 2.303 * \frac{Abs(\lambda) - Abs(600-700)}{0.1}$$

where *Abs* is absorbance at wavelength λ and *Abs* (600-700) is the mean absorbance between 600-700 nm, used to correct the scattering. The 0.1 term represents the optical path length in meters. In this work, absorption coefficients at 254 nm and 320 nm were used to characterize two CDOM fractions with different aromaticity (Campanero et al., 2022; Hansen et al., 2016; Helms et al., 2008); Both absorption coefficients had a measurement error of 0.02 m$^{-1}$.

FDOM was measured using a Perkin Elmer LS-55 spectrofluorometer at selected excitation/emission (Ex/Em) wavelengths (Coble, 1996). The recalcitrant humic-like fluorescence Peaks A (general humic-like substances, 250/435 nm), C (terrestrial humic-like substances, 340/440 nm), and M (marine humic-like substances, 320/410 nm), as well as the labile protein-like Peak T (280/350 nm) were quantified. However,

among the humic-like peaks, only Peak M is presented here due to its strong linear correlations with peaks A and C, based on orthogonal distance regression (Peak M = 1.78 ± 0.01 × Peak A + 0.0040 ± 0.0001, $R^2$ = 0.97; Peak M = 0.99 ± 0.005 × Peak C - 0.00080 ± 0.00005, $R^2$ = 0.99). Fluorescence data were corrected for Raman scatter by subtracting the Milli-Q water blank, which was also used to normalize the fluorescence pair measurements to Raman Units (RU; Murphy et al., 2010). Instrument stability was verified daily with a sealed Milli-Q cuvette along with p-terphenyl and tetraphenyl butadiene fluorescence reference blocks (Starna; Catalá et al., 2015b). In this study, we focus on fluorescence measurements of Peak M and Peak T, with measurement errors of 0.0003 and 0.0004 RU, respectively.

## 2.3 Statistical analysis

In the epipelagic layer (5–200 dbar), depth-integrated average values (± standard error, SE) of temperature, salinity, AOU, FChl-*a*, POCsus, DOC, $a_{CDOM}(254)$, $a_{CDOM}(320)$, Peak M and Peak T, were calculated for waters above and below the pycnocline. These averages were then used to evaluate mesoscale and submesoscale variability, as well as differences at the eddy and station levels, by applying F and T statistical tests. The F-test was first applied to assess whether group variances were equal or different, which determined the appropriate version of the T-test. A $p$-value < 0.05 was considered to indicate significant differences between eddies or stations.

Below the pycnocline (down to 1500 dbar), the variability arising from water mass mixing, physical motion and large-scale biogeochemical processes occurring from the water mass formation areas to the CEC, was separated from the variability associated with local-scale biogeochemical processes using a multiple non-linear regression of each variable (N) against salinity (S), potential temperature (θ), and their squared terms ($S^2$, $\theta^2$), to account for diapycnal mixing (De La Fuente et al., 2014). The coefficient of determination ($R^2$) and the SE of the estimate from these regressions provide insights on: 1) the proportion of variance explained by water mass mixing, physical motion and large-scale biogeochemical processes from the area of formation of the water masses to the CEC, and 2) the magnitude of unexplained variability (residuals) relative to the measurement error of each variable (Álvarez-Salgado et al., 2013). The residuals of those regression (ΔN) represented the variability associated with local biogeochemical processes and are independent of water mass mixing and physical motion processes (De La Fuente et al., 2014; Lønborg and Álvarez-Salgado, 2014). To further explore these local biogeochemical processes, AOU was included as an additional explanatory variable in the multiple regression models of N with S, θ, $S^2$ and $\theta^2$. An increase in $R^2$ and a decrease in the SE are expected when local biogeochemical processes significantly contribute to the variability of a given parameter (Álvarez-Salgado et al., 2013). For those relationships that are significant, the linear regression between ΔN and ΔAOU was assessed, obtaining a regression slope (β ± SE) and its statistical significance. This approach cannot be applied to surface samples (from 5 dbar to the pycnocline) due to the non-conservative behavior of salinity and temperature in the upper ocean.

# 3 Results

## 3.1 Hydrographic variability

A well-defined pycnocline separated the warm surface mixed layer from the underlying subsurface waters in all biogeochemical transects (Figure 2, Supplementary Figure S4A). In the centers of the cyclonic eddies, the pycnocline was shallower -at 10 dbar in Garajonay and 33 dbar in Nublo- while in the anticyclonic Anaga, it was deeper, reaching 139 dbar. The mature Bentayga eddy exhibited a complex structure characteristic of an intrathermocline eddy (Barceló-Llull et al., 2017; Valencia et al., 2025), with the pycnocline showing a concave shape along the horizontal axis at 216 dbar, whereas lighter isopycnals at 89 dbar displayed a slightly convex curvature (Valencia et al., 2025).

Temperature and salinity profiles (Figures 2A, B) revealed warm, saline waters in the anticyclonic eddies and cooler, fresher waters in the cyclonic ones. In Garajonay, 18°C water extended nearly to the surface (Figure 2A). Above the pycnocline, Garajonay and Nublo presented significantly lower temperatures ($p = 1.12 \times 10^{-2}$) and salinities ($p = 2.63 \times 10^{-3}$) compared to Bentayga and Anaga (Table 1). These differences persisted below the pycnocline, where the cyclonic eddies remained notably cooler ($p = 1.23 \times 10^{-7}$) and fresher ($p = 7.54 \times 10^{-4}$).

At the submesoscale, Garajonay's center was ~4°C cooler than surrounding stations above the pycnocline (Stns 15-16; Supplementary Figure S5A). In contrast, the center of Nublo was slightly warmer and Anaga's center slightly cooler than their respective edges in the same layer. Bentayga also exhibited a cooler center above the pycnocline; however, this pattern reversed below the pycnocline, where temperature at Stn 18 reached 22.5 ± 0.44°C -compared to ~20°C in nearby waters (Supplementary Figure S5A, Table 1).

Salinity followed similar trends (Supplementary Figure S5B). Garajonay showed the largest surface-to-depth salinity drop in the epipelagic layer (~0.3 at 200 dbar), indicating the presence of fresher waters at its core. In Nublo, the center of the eddy (Stn 25-28) was saltier than its edges (Stn 23–24 and 29) above the pycnocline. In Anaga, salinity was generally uniform, except for slightly lower values at the edge (Stn 37). In Bentayga, salinity was lowest at the center above the pycnocline and increased outward. This pattern reversed below the pycnocline, where the inner ring exhibited the highest salinity (Table 1).

## 3.2 Chl-*a* and inorganic nutrients

The distribution of CTD-derived FChl-*a* was characterized by a deep chlorophyll maximum (DCM; Figure 2C), which was generally shallower in cyclonic eddies than in anticyclonic ones. Specifically, in Garajonay the DCM was located on average, at ~22 dbar. In Nublo, it was situated below the pycnocline, at approximately ~67 dbar, whereas in Anaga, it was found above the pycnocline, at approximately ~87 dbar. Bentayga exhibited the deepest DCM, averaging ~98 dbar, near the upper pycnocline. Averaging FChl-*a* values within ± 5 dbar of the DCM across the stations of each eddy,

10.3389/fmars.2026.1711689

TABLE 1 Depth-weighted average (± standard error) values of the thermohaline and biogeochemical characteristics (A) above the pycnocline (5 dbar – pycnocline) and (B) below the pycnocline (pycnocline – 200 dbar).

| A) Above the pycnocline (5dbar – pycnocline) | | | | | | | | |
|---|---|---|---|---|---|---|---|---|
| | | Eddies | | | | Bentayga zones | | |
| Variables | Units | Garajonay | Nublo | Anaga | Bentayga | Core | Inner ring | Outer ring |
| | | 17 -19 | 24-29 | 31-37 | 12-26 | 15-20 | 13-14 + 21-23 | 12 + 24-26 |
| *Temp.Potential* | °C | *18.94 ± 0.13* | *22.40 ± 0.08* | *22.83 ± 0.06* | *22.98 ± 0.05* | *22.75 ± 0.06* | *23.08 ± 0.07* | *23.42 ± 0.02* |
| *Salinity* | | *36.537 ± 0.007* | *36.653 ± 0.003* | *36.804 ± 0.002* | *36.764 ± 0.004* | *36.715 ± 0.005* | *36.783 ± 0.004* | *36.814 ± 0.003* |
| *AOU* | *µmol kg$^{-1}$* | *-12.8 ± 2.8* | *-6.3 ± 0.3* | *-8.1 ± 0.2* | *-1.9 ± 0.3* | *1.8 ± 0.5* | *-2.7 ± 0.4* | *-6.5 ± 0.2* |
| DIN | µmol L$^{-1}$ | 0.75 ± 0.31 | 0.22 ± 0.02 | 0.67 ± 0.17 | 0.36 ± 0.14 | 0.36 ± 0.13 | 0.40 ± 0.16 | 0.31 ± 0.15 |
| $PO_4^{3-}$ | µmol L$^{-1}$ | 0.08 ± 0.02 | 0.05 ± 0.01 | 0.07 ± 0.01 | 0.08 ± 0.01 | 0.10 ± 0.02 | 0.09 ± 0.01 | 0.06 ± 0.01 |
| $SiO_4^{4-}$ | µmol L$^{-1}$ | 2.19 ± 0.07 | 1.42 ± 0.04 | 2.17 ± 0.09 | 2.15 ± 0.08 | 2.25 ± 0.08 | 2.07 ± 0.07 | 2.12 ± 0.10 |
| DOC | µmol L$^{-1}$ | 78.3 ± 2.6 | 77.7 ± 2.4 | 69.2 ± 1.7 | 70.6 ± 2.3 | 70.7 ± 2.5 | 69.6 ± 2.1 | 71.9 ± 2.1 |
| POCsus | µmol L$^{-1}$ | 14.1 ± 1.3 | 4.3 ± 0.4 | 2.7 ± 0.4 | 2.5 ± 0.3 | 2.3 ± 0.2 | 2.5 ± 0.3 | 2.5 ± 0.2 |
| $a_{CDOM}(254)$ | m$^{-1}$ | 1.21 ± 0.01 | 1.32 ± 0.01 | 1.26 ± 0.01 | 1.25 ± 0.01 | 1.24 ± 0.01 | 1.23 ± 0.01 | 1.28 ± 0.01 |
| $a_{CDOM}(320)$ | m$^{-1}$ | 0.21 ± 0.01 | 0.20 ± 0.01 | 0.16 ± 0.01 | 0.15 ± 0.01 | 0.15 ± 0.01 | 0.14 ± 0.01 | 0.16 ± 0.01 |
| Peak M | 10$^{-3}$ RU | 7.2 ± 0.3 | 5.4 ± 0.9 | 5.0 ± 0.6 | 5.2 ± 1.0 | 5.2 ± 1.0 | 5.0 ± 1.1 | 5.3 ± 0.9 |
| Peak T | 10$^{-3}$ RU | 10.6 ± 0.6 | 8.6 ± 0.3 | 7.4 ± 0.3 | 7.7 ± 0.4 | 8.2 ± 0.4 | 7.3 ± 0.4 | 7.5 ± 0.4 |
| B) Below the pycnocline (pycnocline – 200 dbar) | | | | | | | | |
| *Temp.Potential* | °C | *15.99 ± 0.07* | *17.94 ± 0.10* | *19.17 ± 0.09* | *20.01 ± 0.08* | *20.69 ± 0.06* | *19.77 ± 0.08* | *19.28 ± 0.12* |
| *Salinity* | | *36.202 ± 0.012* | *36.556 ± 0.015* | *36.749 ± 0.008* | *36.712 ± 0.006* | *36.705 ± 0.004* | *36.736 ± 0.004* | *36.693 ± 0.011* |
| *AOU* | *µmol kg$^{-1}$* | *57.6 ± 1.3* | *24.1 ± 1.4* | *9.8 ± 0.9* | *14.0 ± 0.7* | *6.8 ± 0.2* | *10.5 ± 0.4* | *29.4 ± 1.6* |
| DIN | µmol L$^{-1}$ | 9.55 ± 2.57 | 4.12 ± 1.22 | 2.72 ± 0.87 | 2.57 ± 0.60 | 1.69 ± 0.28 | 2.12 ± 0.45 | 4.44 ± 1.29 |
| $PO_4^{3-}$ | µmol L$^{-1}$ | 0.51 ± 0.13 | 0.23 ± 0.06 | 0.15 ± 0.05 | 0.20 ± 0.02 | 0.19 ± 0.01 | 0.16 ± 0.01 | 0.26 ± 0.05 |
| $SiO_4^{4-}$ | µmol L$^{-1}$ | 4.92 ± 0.81 | 2.31 ± 0.28 | 2.51 ± 0.23 | 2.46 ± 0.14 | 2.36 ± 0.07 | 2.30 ± 0.11 | 2.83 ± 0.28 |
| DOC | µmol L$^{-1}$ | 54.5 ± 6.1 | 66.1 ± 2.8 | 61.3 ± 1.7 | 60.9 ± 2.1 | 58.6 ± 2.0 | 62.5 ± 1.9 | 62.5 ± 2.3 |
| POCsus | µmol L$^{-1}$ | 2.5 ± 2.7 | 2.2 ± 0.5 | 1.6 ± 0.3 | 1.4 ± 0.2 | 1.4 ± 0.3 | 1.4 ± 0.2 | 1.4 ± 0.2 |
| $a_{CDOM}(254)$ | m$^{-1}$ | 1.01 ± 0.05 | 1.12 ± 0.05 | 1.12 ± 0.04 | 1.15 ± 0.03 | 1.16 ± 0.03 | 1.15 ± 0.02 | 1.14 ± 0.05 |
| $a_{CDOM}(320)$ | m$^{-1}$ | 0.18 ± 0.01 | 0.20 ± 0.01 | 0.18 ± 0.01 | 0.18 ± 0.01 | 0.18 ± 0.01 | 0.18 ± 0.01 | 0.20 ± 0.01 |
| Peak M | 10$^{-3}$ RU | 11.3 ± 1.0 | 9.5 ± 0.7 | 8.6 ± 0.6 | 10.2 ± 0.5 | 9.8 ± 0.3 | 10.1 ± 0.4 | 11.0 ± 0.8 |
| Peak T | 10$^{-3}$ RU | 6.1 ± 1.1 | 7.3 ± 0.5 | 7.0 ± 0.5 | 7.5 ± 0.4 | 7.8 ± 0.4 | 7.3 ± 0.2 | 7.3 ± 0.5 |

Potential temperature, salinity and apparent oxygen utilization (AOU) has a vertical resolution of 1 db (in italics). Stations within each eddy "Garajonay", "Nublo", "Anaga" and "Bentayga" are indicated. For this last, the three zones within the eddy are also shown independently: the core, the inner ring and the outer ring.

we found that Garajonay exhibited the highest mean FChl-*a* concentration (4.06 ± 0.35 µg L$^{-1}$), with its center reaching a depth-weighted average of 6.89 ± 0.65 µg L$^{-1}$ (Supplementary Figure S6A). In Nublo, the mean FChl-*a* was 0.86 ± 0.05 µg L$^{-1}$, whereas in Anaga it was lower (0.47 ± 0.02 µg L$^{-1}$). Bentayga presented the lowest average FChl-*a* concentration among all eddies (0.27 ± 0.02 µg L$^{-1}$).

Nutrient distributions (Supplementary Figures S7A–C) in the epipelagic layer (< 200 dbar), differed above and below the pycnocline across the eddies (Table 1). Above the pycnocline, Garajonay exhibited the highest DIN concentrations. Below the pycnocline, Garajonay again stood out, showing the highest DIN concentration (9.55 ± 2.57 µmol L$^{-1}$), followed by Nublo, the other cyclonic eddy. $PO_4^{3-}$ concentration above the pycnocline ranged from 0.05 to 0.08 µmol L$^{-1}$ (Table 1), with no significant differences among eddies. Below the pycnocline, concentration was <0.25 µmol L$^{-1}$ in all cases except Garajonay (0.51 ± 0.13 µmol L$^{-1}$), which was significantly higher than Bentayga ($p$ = 4.06·10$^{-4}$) and Nublo ($p$ = 3.32·10$^{-4}$). Moreover, Nublo showed significantly higher concentrations than Anaga ($p$ = 8.14·10$^{-3}$). Minimum average $SiO_4^{4-}$ concentration above the pycnocline was observed in Nublo (1.42 ± 0.04 µmol L$^{-1}$; Table 1), significantly lower than in Garajonay ($p$ = 2.38·10$^{-2}$) and Anaga ($p$ = 1.42·10$^{-3}$). Below the pycnocline, Garajonay showed the maximum concentration (4.92 ± 0.81 µmol L$^{-1}$), whereas the other eddies ranged between 2.30 and 2.50 µmol L$^{-1}$. Significant differences were found only between Garajonay and Bentayga ($p$ = 3.12·10$^{-8}$) and Garajonay and Nublo ($p$ = 2.24·10$^{-5}$).

In the mesopelagic layer (> 200 dbar), nutrient concentrations generally increased progressively with depth. However, in Anaga

and Bentayga, nutrient concentrations below 500 m were lower, with values in Anaga remaining reduced down to more than 1250 m, reflecting the influence of the intense anticyclonic eddy.

Submesoscale nutrient variability (not shown) revealed significant differences between stations. Above the pycnocline, this variability was observed only in Bentayga, where the outer ring had lower $PO_4^{3-}$, than the inner and core rings (Table 1). Below the pycnocline, differences occurred at the Nublo-Anaga front: Nublo exhibited higher $PO_4^{3-}$ and DIN than the stations at the frontal boundary (Stns 30-31), while Anaga had higher $SiO_4^{4-}$ than its frontal stations (Stns 29-30). Additionally, the outer ring of Bentayga below the pycnocline showed higher $PO_4^{3-}$ than its inner and core rings.

## 3.3 Apparent oxygen utilization

The 0 μmol $kg^{-1}$ AOU isoline (Figure 3A) coincided with the pycnocline in all eddies, except in Bentayga, where it followed the previously described slight convex shape. This isoline was shallowest in Garajonay (14 dbar) and progressively deepened in Nublo (59 dbar), Bentayga (86 dbar), and Anaga (145 dbar). In Bentayga, a distinct region of elevated AOU was observed below the pycnocline (150-300 dbar) in the outer ring. In the mesopelagic layer, AOU exhibited a vertical pattern similar to that of nutrients, increasing with depth. Consistent with the nutrient distributions, AOU values in Anaga and Bentayga were lower than in the surrounding waters, reflecting the influence of the anticyclonic eddies.

Above the pycnocline, AOU values were negative across all eddies (Table 1), with cyclonic eddies Garajonay and Nublo showing significantly lower values ($p = 1.73 \times 10^{-2}$). Garajonay presented the lowest AOU (-12.8 ± 2.8 μmol $kg^{-1}$), followed by Anaga (-8.1 ± 0.2 μmol $kg^{-1}$), Nublo (-6.3 ± 0.3 μmol $kg^{-1}$) and Bentayga, which had the highest AOU (-1.9 ± 0.3 μmol $kg^{-1}$). Below the pycnocline, this pattern reversed: cyclonic eddies displayed significantly higher positive AOU values ($p = 6.25 \times 10^{-3}$), with Garajonay at 57.6 ± 1.3 μmol $kg^{-1}$ and Nublo at 24.1 ± 1.4 μmol $kg^{-1}$, compared to 14.0 ± 0.7 μmol $kg^{-1}$ in Bentayga and 9.8 ± 0.9 μmol $kg^{-1}$ in Anaga.

At the submesoscale, the lowest AOU value was found at the center of Garajonay (Stn 18, -17.0 ± 1.9 μmol $kg^{-1}$; Supplementary Figure S6B). In Nublo and Anaga, more negative AOU values were observed at the frontal region (Stns 29-31) and peripheral stations. In Bentayga, AOU was least negative above the pycnocline and displayed clear intra-ring variability. AOU decreased from the eddy core to the outer ring above the pycnocline, whereas it increased from the core toward the outer ring below the pycnocline (Table 1).

A multiple non-linear regression of AOU with temperature and salinity explained 96% of AOU variability from the pycnocline to 1500 dbar, with a SE of 10.5 μmol $kg^{-1}$ (Eq.1 in Table 2). The difference between the observed and predicted AOU from the multiple linear regression (ΔAOU) represents the variability of AOU not explained by water mass mixing physical motion and

TABLE 2 Parameters of the linear mixing and mixing-biogeochemical regression models for apparent oxygen utilization (AOU; μmol $kg^{-1}$), dissolved organic carbon (DOC; μmol $L^{-1}$), suspended particulate organic carbon (POCsus; μmol $L^{-1}$), CDOM absorption at 254 nm ($a_{CDOM}(254)$; $m^{-1}$), CDOM absorption at 320 nm ($a_{CDOM}(320)$; $m^{-1}$), and fluorescence at excitation/emission pairs 320/410 nm (Peak M; RU) and 280/350 nm (Peak T; RU), based on samples collected below the pycnocline (from the pycnocline to 1500 dbar).

| $N_1$ | $N_2$ | Eq | $R^2$ | SE | % SE reduction | $\beta$ (± SE) | $p$ | n |
|---|---|---|---|---|---|---|---|---|
| AOU | | 1 | 0.96 | 10.5 | | | | 605 |
| DOC | | 2 | 0.68 | 5.3 | | | | 590 |
| DOC | AOU | 3 | 0.69 | 5.2 | 1.69 | -0.50 ± 0.11 | $5.27 \times 10^{-6}$ | 590 |
| POCsus | | 4 | 0.20 | 1.6 | | | | 574 |
| POCsus | AOU | 5 | 0.29 | 1.5 | 5.81 | -0.15 ± 0.01 | $9.88 \times 10^{-16}$ | 574 |
| $a_{CDOM}(254)$ | | 6 | 0.89 | 0.054 | | | | 594 |
| $a_{CDOM}(254)$ | AOU | 7 | 0.91 | 0.049 | 9.09 | -0.0051 ± 0.0005 | $4.07 \times 10^{-26}$ | 594 |
| $a_{CDOM}(320)$ | | 8 | 0.05 | 0.025 | | | | 594 |
| $a_{CDOM}(320)$ | AOU | 9 | 0.05 | 0.025 | 0.40 | – | 0.08 | 594 |
| Peak M | | 10 | 0.86 | 0.00104 | | | | 603 |
| Peak M | AOU | 11 | 0.88 | 0.00097 | 7.21 | 0.000099 ± 0.000010 | $2.02 \times 10^{-21}$ | 603 |
| Peak T | | 12 | 0.53 | 0.00117 | | | | 602 |
| Peak T | AOU | 13 | 0.58 | 0.00111 | 5.13 | -0.000111 ± 0.000013 | $1.15 \times 10^{-15}$ | 602 |

For each variable, the coefficient of determination ($R^2$), estimation standard error (SE), the percentage reduction in SE of the mixing-biogeochemical model compared to the linear mixing model and its sample size (n) are reported. The regression coefficient β (± SE) represents the relationship between $N_1$ and $N_2$ independent of mixing; $p$ indicates the statistical significance of β.

10.3389/fmars.2026.1711689

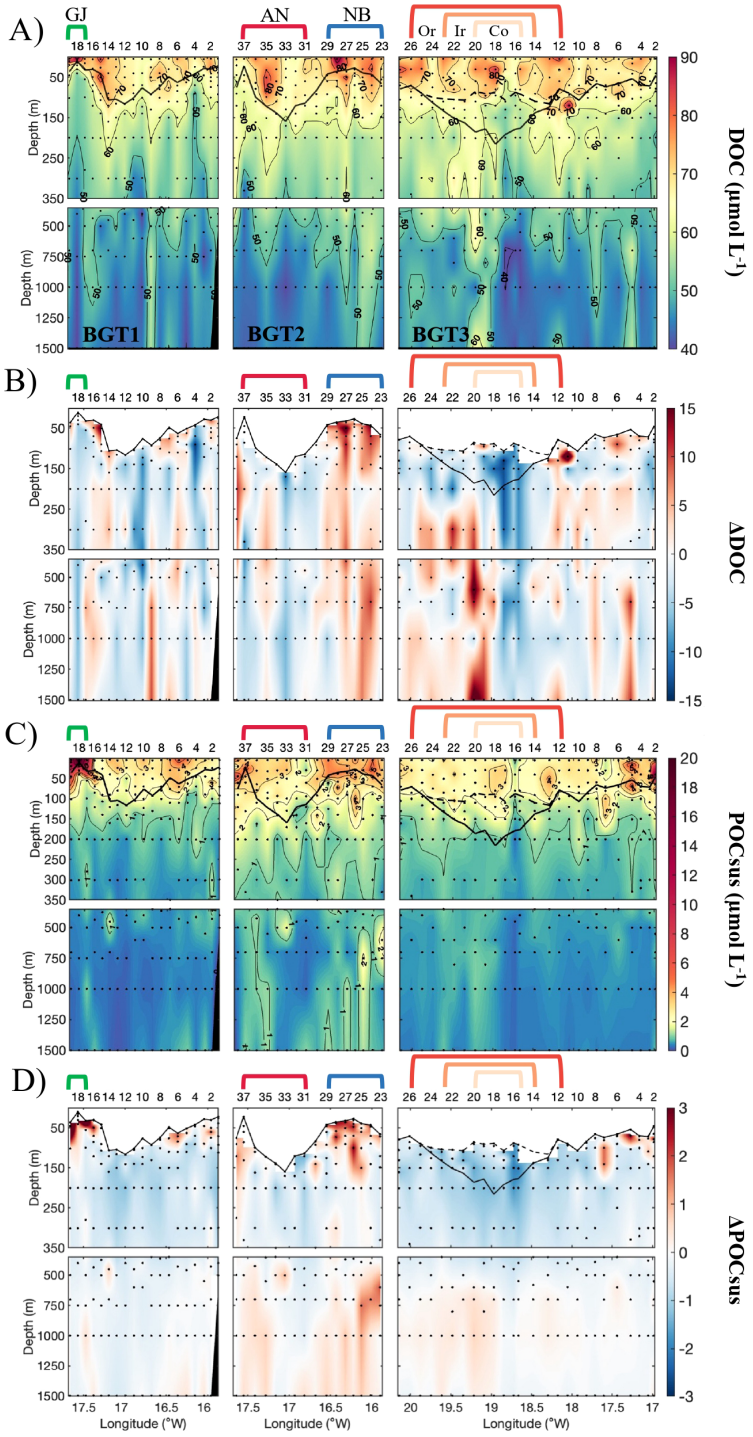


FIGURE 4
Vertical distributions of **(A)** dissolved organic carbon (DOC) and **(C)** suspended particulate organic carbon (POCsus), both in µmol $L^{-1}$, and their corresponding residuals in **(B)** ΔDOC and **(D)** ΔPOCsus. Each box, along the horizontal axis, represents one of the biogeochemical transects (BGT1, BGT2, BGT3; left to right). Note that the BGT3 POCsus distribution is estimated. Colored brackets indicate the presence of eddies Garajonay (GJ; green), Anaga (AN; red), Nublo (NB; blue), and Bentayga (orange tones). For Bentayga, the core (Co), inner ring (Ir) and outer ring (Or) are distinguished. Pycnoclines are shown as thick black lines; in Bentayga, a dashed line marks the upper pycnocline and the boundary of the low-salinity core.

large-scale biogeochemical processes, i.e., the contribution of local biogeochemical processes to AOU variability. ΔAOU was positive below the pycnocline in all eddies, with greater vertical extent in the mature eddies Garajonay and Bentayga (Figure 3B).

## 3.4 Dissolved organic carbon

DOC concentrations mostly ranged from 45 to 70 µmol $L^{-1}$, with a few surface hotspots exceeding 80 µmol $L^{-1}$ (Figure 4A).

Above the pycnocline, cyclonic eddies showed higher DOC (>76 μmol $L^{-1}$) than anticyclonic ones (~70 μmol $L^{-1}$) (Table 1). Below the pycnocline, Garajonay had significantly lower DOC than Nublo ($p = 1.19 \times 10^{-3}$) and Bentayga ($p = 7.43 \times 10^{-3}$). Vertical DOC "plumes" extending below 500 dbar were observed at several stations (Figure 4A).

At the submesoscale, the center of Garajonay exhibited maximum DOC concentration (88.1 ± 2.0 μmol $L^{-1}$; Supplementary Figure S8A). Above the pycnocline, DOC was significantly lower at the Nublo-Anaga front (Stns 30-31; $p = 1.16 \times 10^{-2}$) compared to Nublo. Bentayga presented significant DOC intra-eddy differences only below the pycnocline, where its core ring had a lower concentration (58.6 ± 2.0 μmol $L^{-1}$; $p = 4.23 \times 10^{-2}$) than the other two rings.

The multiple non-linear regression with temperature and salinity explained 68% of the DOC variability below the pycnocline, with a SE of 5.3 μmol $L^{-1}$ (Eq.2 in Table 2). Similar to AOU, the difference between the observed and predicted DOC from the multiple linear regression (ΔDOC) represents the variability of DOC associated with local biogeochemical processes. In this context, ΔDOC presented negative values in Garajonay and Anaga (Figure 4B), whereas Nublo displayed vertical plume-like structures of positive ΔDOC extending from the pycnocline down to 1500 dbar. In Bentayga, ΔDOC values were predominantly negative near the pycnocline, at most stations (Stns 13-18). Below the pycnocline, however, the pattern shifted, with positive values observed from Stn 18 to 26. When AOU was included in the multiple linear regression model for DOC below the pycnocline (**Eq.3 in** Table 2), a significant ΔDOC/ΔAOU slope (β) of -0.50 ± 0.11 mol C mol $O_2^{-1}$ ($p = 5.27 \times 10^{-6}$) was obtained.

## 3.5 Suspended particulate organic carbon

POCsus along BGT1 and BGT2 showed higher concentrations above the pycnocline in all eddies, with some vertical column-like structures of slightly higher concentration extending below the pycnocline (Figure 4C). In Bentayga, Stn 16 showed the lowest POCsus values. Garajonay presented the highest average concentrations (Table 1) and Nublo showed significantly ($p = 2.25 \times 10^{-3}$) higher POCsus (4.3 ± 0.4 μmol $L^{-1}$) than Anaga (2.7 ± 0.4 μmol $L^{-1}$). Below the pycnocline, cyclonic eddies showed significantly higher POCsus concentrations.

At the submesoscale, above the pycnocline, Garajonay exhibited elevated POCsus concentrations, particularly at its center, with values exceeding 20 μmol $L^{-1}$ (Supplementary Figure S8B). Nublo also showed slightly higher POCsus average levels compared to Anaga. Below the pycnocline, the center of Nublo exhibited the highest average POCsus, whereas Anaga generally displayed very low concentrations throughout.

The multiple non-linear regression with salinity and temperature indicates that 20% of the POCsus variability was explained by water mass mixing, physical motion and large-scale biogeochemical processes (SE 1.6 μmol $L^{-1}$; Eq.4 in Table 2). The residuals of the multiple linear regression (ΔPOCsus) vary with local biogeochemical processes, presenting strong positive values beneath Garajonay and Nublo, primarily near the pycnocline (Figure 4D). Slightly positive values were also observed near the pycnocline at the western edge of Anaga (Stns 36 and 37), as well as in the mesopelagic layer at several BGT2 stations. In Bentayga, the estimated ΔPOCsus values were predominantly negative throughout both the epipelagic and mesopelagic layers. The eastern half of the halostad exhibited the most negative values. When AOU was included in the multiple linear regression model for POCsus below the pycnocline (Eq.5 in Table 2), a significant ΔPOCsus/ΔAOU slope (β) of -0.15 ± 0.01 mol C mol $O_{2-}^{1}$ was obtained.

## 3.6 Chromophoric dissolved organic matter

$a_{CDOM}(254)$, a proxy for the abundance of conjugated double bonds in DOC (Lønborg and Álvarez-Salgado, 2014; Weishaar et al., 2003), was higher above the pycnocline and decreased sharply with depth (Figure 5A). Among the cyclonic eddies, Nublo exhibited significantly higher average $a_{CDOM}(254)$ values than Garajonay, both above ($p = 1.16 \times 10^{-2}$) and below the pycnocline ($p = 7.96 \times 10^{-3}$; Table 1). In addition, $a_{CDOM}(254)$ in Garajonay below the pycnocline was significantly lower than in Bentayga ($p = 2.83 \times 10^{-4}$).

At the submesoscale, Stns 15-16 (the frontal region between Garajonay and Anaga) showed slightly higher $a_{CDOM}(254)$ than the core of Garajonay (Supplementary Figure S9A), both above ($p = 2.88 \times 10^{-2}$) and below the pycnocline ($p = 1.34 \times 10^{-2}$). Additional intra-eddy differences were observed in Nublo, particularly at its eastern (Stns 23-24) and western (Stns 27-29) edges, where $a_{CDOM}(254)$ was higher above the pycnocline, while the eddy center exhibited lower average values below it. In Anaga, higher $a_{CDOM}(254)$ were observed above the pycnocline, primarily in the eastern part of the eddy. In contrast, Bentayga exhibited no significant intra-eddy differences in the epipelagic layer.

The multiple non-linear correlation with the thermohaline properties explained 89% of the $a_{CDOM}(254)$ variability, from the pycnocline to 1500 dbar (SE of 0.054 $m^{-1}$; Eq.6 in Table 2). The distribution of $\Delta a_{CDOM}(254)$ (Figure 5B) in Garajonay displayed slightly negative values above 300 dbar and strongly negative values below that depth. In Nublo, strong positive values appear near the pycnocline and extend downward to 1500 dbar, forming vertical column-like structures. Although Anaga was primarily characterized by negative values, it also presented a column of positive values at Stn 32, extending from the pycnocline to 450 dbar. In Bentayga, values were low near the pycnocline, but columns of positive values extended into the mesopelagic layer. Incorporation of AOU into this multiple linear regression model, improved the goodness of the fit and further reduced the SE (Eq.7 in Table 2). A significant $\Delta a_{CDOM}(254)/\Delta AOU$ slope of $-0.0051 \pm 0.0005$ $m^{-1}$ kg $\mu mol^{-1}$ was obtained.

$a_{CDOM}(320)$, a proxy for aromatic DOM compounds (Nelson et al., 2004), generally showed lower values at the surface and slightly higher at depth (Figure 5C). Nublo and Garajonay exhibited significantly higher $a_{CDOM}(320)$ values than Anaga ($p = 1.31 \times 10^{-2}$)

10.3389/fmars.2026.1711689

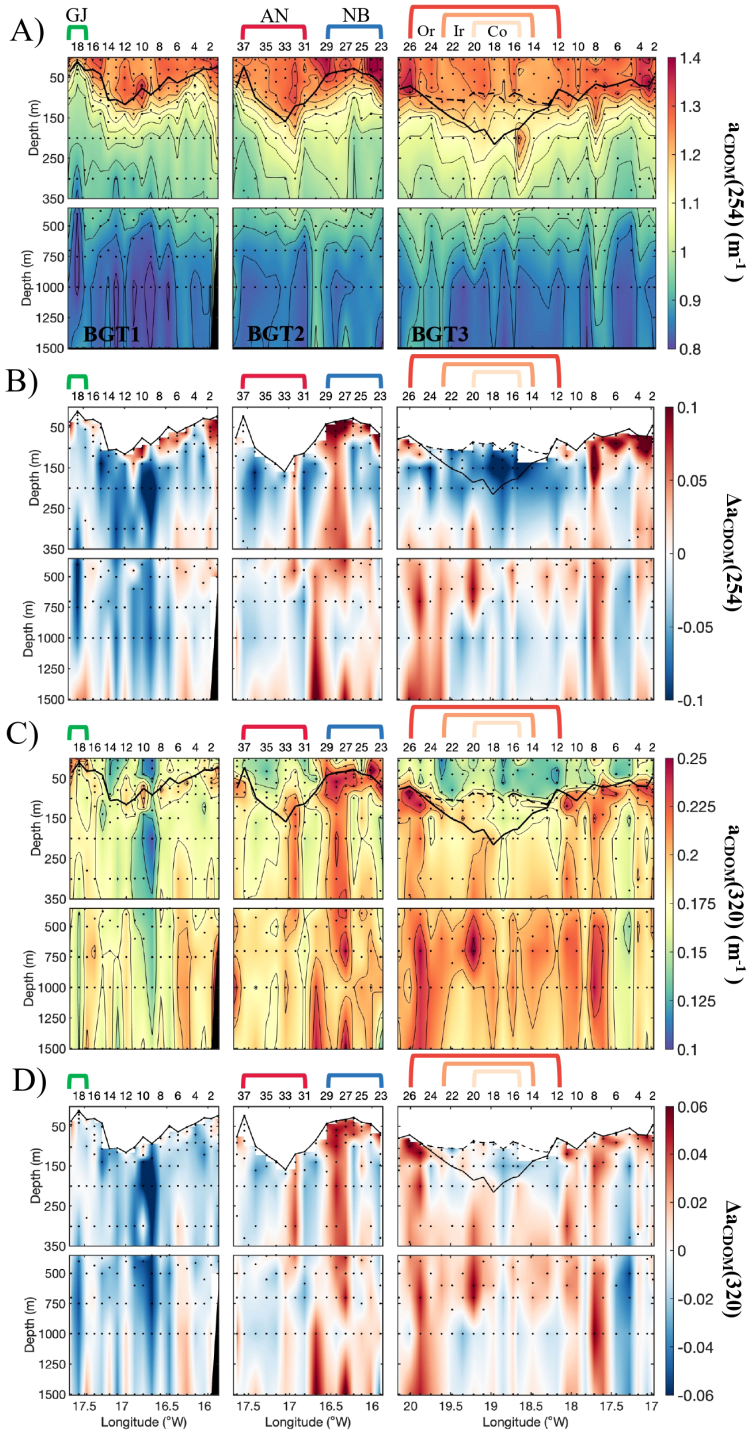


FIGURE 5
Vertical distributions of **(A)** absorption coefficient at 254 nm and **(C)** at 320 nm, both in $m^{-1}$ and their corresponding residuals in **(B)** $\Delta a_{CDOM}(254)$ and **(D)** $\Delta a_{CDOM}(320)$. Each box, along the horizontal axis, represents one of the biogeochemical transects (BGTI, BGT2, BGT3; left to right). Colored brackets indicate the presence of eddies-Garajonay (GJ: green), Anaga (AN; red), Nublo (NB; blue), and Bentayga (orange tones). For Bentayga, the core (Co), inner ring (Ir) and outer ring (Or) are distinguished. Pycnoclines are shown as thick black lines; in Bentayga, a dashed line marks the upper pycnocline and the boundary of the low- salinity core.

and Bentayga ($p = 4.00 \times 10^{-4}$), respectively (Table 1). Below the pycnocline, Garajonay recorded the lowest $a_{CDOM}(320)$, which was significantly lower than that observed in Nublo ($p = 4.62 \times 10^{-2}$).

At the submesoscale, Garajonay displayed significantly higher $a_{CDOM}(320)$ values above the pycnocline compared to the adjacent stations Stns 15-16 ($p = 9.22 \times 10^{-3}$; Supplementary Figure S9B). In Nublo, elevated concentrations were detected above the pycnocline at the edges (Stns 24 and 29), while below the pycnocline, the western half (Stns 27-29) showed higher $a_{CDOM}(320)$. In Anaga, the highest values were located at the eddy center (Stns 32-33) in both the upper and deeper layers. In contrast, Bentayga displayed no clear $a_{CDOM}(320)$ variability across eddy rings or depths.

10.3389/fmars.2026.1711689

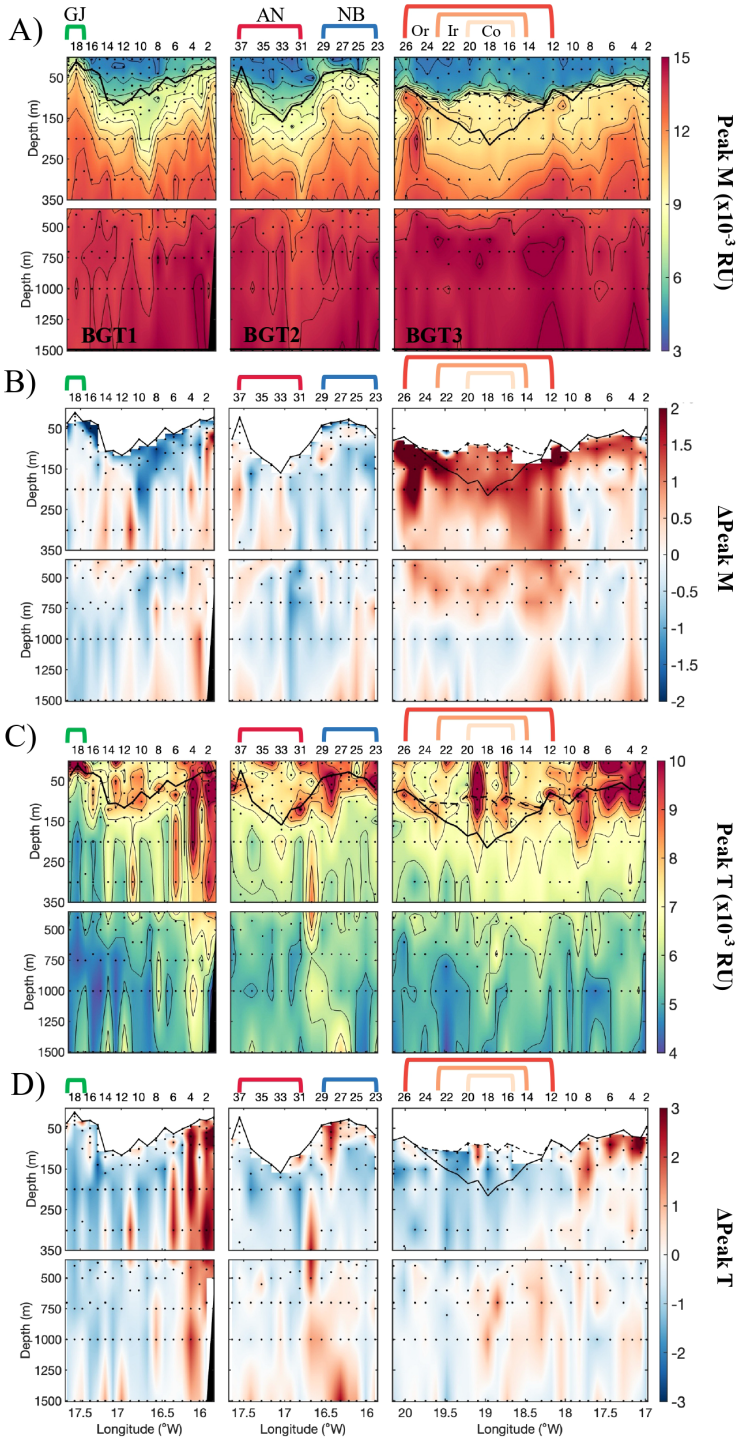


FIGURE 6
Vertical distributions of fluorescence at Ex/Em **(A)** pair 320/410 nm (Peak M) and **(C)** pair 280/350 nm (Peak T), both in $\times 10^{-3}$ RU, and their corresponding residuals in **(B)** ΔPeak M and **(D)** ΔPeak T. Each box, along the horizontal axis, represents one of the biogeochemical transects (BGT1, BGT2, BGT3; left to right). Colored brackets indicate the presence of eddies-Garajonay (GJ; green), Anaga (AN; red), Nublo (NB; blue), and Bentayga (orange tones). For Bentayga, the core (Co), inner ring (Ir) and outer ring (Or) are distinguished. Pycnoclines are shown as thick black lines; in Bentayga, a dashed line marks the upper pycnocline and the boundary of the low-salinity core.

Only 5% of the $a_{CDOM}(320)$ variability was explained by the multiple non-linear regression with salinity and temperature (Eq.8 in Table 2); and the model did not improve with the inclusion of AOU (Eq.9 inTable 2). The distribution of $\Delta a_{CDOM}(320)$ (Figure 5D) closely resembled that of $\Delta a_{CDOM}(254)$ (Figure 5B) for every eddy except Bentayga, where slight negative values were observed between the pycnocline and 200 dbar. Below that depth, broader columns of positive $\Delta a_{CDOM}(320)$ values appeared (Figure 5D).

### 3.7 Fluorescent dissolved organic matter

Peak M generally increased with depth (Figure 6A), with particularly high levels at the western edges of Anaga (Stn 37 and 28) and Bentayga (Stn 25-27). This peak M hotspot in Bentayga was found between 100 and 300 dbar and coincided with the maximum observed in AOU (Figure 3A). Above the pycnocline, Garajonay presented the highest average Peak M values (Table 1), significantly higher than in Bentayga ($p = 4.70{\cdot}10^{-3}$ and Nublo, $p = 6.82 \times 10^{-3}$). Below the pycnocline, significant differences were observed depending on the type of eddy. Garajonay showed the highest fluorescence, significantly higher than Bentayga ($p = 2.67 \times 10^{-3}$). Nublo also exhibited a significantly higher concentration than Anaga ($p = 4.79 \times 10^{-4}$). Similar patterns emerged when comparing the lifespan of the eddies: the older eddies had higher concentrations than the younger ones ($p = 1.10 \times 10^{-3}$ between Garajonay and Nublo, and $p = 8.87 \cdot 10^{-5}$ between Bentayga and Anaga).

At the submesoscale, Garajonay presented similar Peak M values above the pycnocline and a maximum below the pycnocline at Stn 18 (Supplementary Figure S10A). This resulted in significantly higher Peak M fluorescence above the pycnocline within the eddy compared to the Garajonay-Anaga front (Stns 15-16; $p = 3.02 \times 10^{-3}$). The Nublo-Anaga pair showed contrasting patterns above the pycnocline: while most stations in Anaga had similar Peak M values, Nublo displayed lower values at its center compared to its edges. Below the pycnocline, Nublo had higher average Peak M values (Table 1), leading to significant differences with the Nublo-Anaga front stations (Stns 30-31), which showed lower values ($p = 1.57 \times 10^{-4}$). Within Bentayga, Peak M values were constant above the pycnocline (Supplementary Figure S10A; Table 1), whereas below it, concentrations increased from the center toward the periphery. However, these differences were not significant.

The multiple non-linear regression with salinity and temperature indicates that 86% of Peak M variability from the pycnocline to 1500 dbar can be attributed to water mass mixing, physical motion and large-scale biogeochemical processes, with a SE of $1.04 \times 10^{-3}$ RU (Eq.10 in Table 2). The distribution of ΔPeak M (Figure 6B), related to local biogeochemical processes, showed slightly negative values within the cyclonic eddies. In Anaga, slightly positive ΔPeak M values were observed in column-like structures below its center (Stn 33, pycnocline - 400 dbar) and western edge (Stn 37, pycnocline - 750 dbar). Bentayga exhibited the highest ΔPeak M values from the pycnocline to 700 dbar, with the most elevated values found at shallower depths. Notably, the spatial distribution of ΔPeakM closely resembled that of ΔAOU (Figure 4B), particularly in Bentayga. Including AOU in the multiple linear regression improved the model fit, reduced the SE (Eq.11 in Table 2) and yielded a significant ΔPeakM/ΔAOU slope of $9.9 \pm 1.0 \times 10^{-5}$ RU $kg^{-1}$ μmol.

Protein-like fluorescence (Peak T) showed elevated concentrations above the pycnocline in the cyclonic eddies and in the central ring of Bentayga (Figure 6C; Table 1). Significant differences were found only between Garajonay and Bentayga ($p = 4.42 \times 10^{-2}$), with Garajonay exhibiting higher Peak T values than Bentayga. Below the pycnocline, concentrations were generally uniform ($7\text{-}7.5 \times 10^{-3}$ RU), except in Garajonay, which presented significantly lower values ($6.1 \pm 1.1 \times 10^{-3}$ RU) compared to Nublo ($p = 1.57 \times 10^{-2}$) and Bentayga ($p = 1.65 \times 10^{-4}$).

At the submesoscale (Supplementary Figure S10B), the eddy center in Garajonay was characterized by higher Peak T values ($12.1 \pm 0.5 \times 10^{-3}$ RU on average) compared to stations 15-16, indicating lower concentrations at the front ($p = 3.23 \times 10^{-2}$). Within Garajonay, the eddy center highlights above the pycnocline, because it reached a maximum average value of $12.1 \pm 0.5 \times 10^{-3}$ RU. Nublo displayed elevated Peak T average values above the pycnocline at all stations except Stn 25, while below the pycnocline higher values were observed between Stns 26-29. In Anaga, Peak T remained relatively stable above and below the pycnocline. In Bentayga, although two Peak T maxima were observed above the pycnocline near the eddy center (Stns 16 and 19), these differences were not significant.

The multiple non-linear regression with salinity and temperature accounted for 53% of the variability in Peak T (SE = $1.17 \times 10^{-3}$ RU; Eq.12 in Table 2). ΔPeakT distribution (Figure 6D) showed that Garajonay and Anaga were predominantly characterized by negative residuals, whereas Nublo exhibited positive values just below the pycnocline and at depths >350 dbar. In contrast, Bentayga displayed mostly negative residuals, except for a localized positive anomaly at Stn 19 just below the pycnocline, and slightly positive values at depths >350 m from Stns 12 to 19. When including AOU, the multiple linear regression increased the explained variance to 58% and reduced the SE by 5.1% (Eq.13 in Table 2). Moreover, a significant ΔPeakT/ΔAOU slope of $-11.1 \pm 1.3 \times 10^{-5}$ RU $kg^{-1}$ μmol was obtained.

## 4 Discussion

In this study, we investigated at high spatial resolution the influence of island-induced mesoscale and submesoscale eddies on the distributions of dissolved and suspended particulate organic matter in the Canary region. Our aim was to advance our understanding of how these eddies affect the biological carbon pump across different stages of their life cycle. The results presented here may be extrapolated to other cyclonic and anticyclonic mesoscale eddies in different oceanic regions, thereby offering broader insights into their biogeochemical roles.

### 4.1 Eddies sampled at different life stages

At the western end of BGT1 (Figure 1B), a small cyclonic eddy (~25 km diameter), named Garajonay, was detected. This feature was classified as a submesoscale eddy because its horizontal scale was smaller than the local internal Rossby radius of deformation (~40 km), as first estimated for this region by Chelton et al. (1998). Satellite imagery indicated that Garajonay formed in mid-July, approximately one month prior to sampling, between the islands of La Gomera and El Hierro, a well-known hotspot for eddy generation (Arístegui et al., 2003; Barton and Arístegui, 2004; Sangrà et al., 2009). Its size is comparable to that of La Gomera

Island, consistent with previous observations that island-induced eddies often exhibit spatial scales like those of the islands from which they originate (Cardoso et al., 2020; Sangrà et al., 2009).

Garajonay was flanked to the northwest and southeast by two positive sea level anomalies, indicative of anticyclonic regions (Figure 1B), including eddy Anaga, forming two distinct fronts, and was further constrained by the surrounding islands. This configuration of several closely spaced eddies has been previously observed in the Canary region (e.g. Arístegui et al., 2003; Hernández-Hernández et al., 2020), as well as in other oceanic regions, including the Bering Sea (Mizobata et al., 2002), the South China Sea (Wang et al., 2017), the Cabo Verde Archipelago (Cardoso et al., 2020), the East Australian Current region (Chen et al., 2021), the southeastern Mediterranean Sea (Belkin et al., 2022), and the southern Indian Ocean (Ding et al., 2024). The succession of different types of eddies can enhance vertical pumping by disrupting geostrophic balance, while the associated fronts may generate ageostrophic secondary circulation through the convergence of water masses with different densities. These processes influence both vertical and horizontal velocities, thereby redistributing organic matter and plankton (Arístegui et al., 2003; Arístegui and Montero, 2005; Baltar et al., 2009; Hernández-Hernández et al., 2020). Such mechanisms may explain the elevated concentrations of Chl-*a*, POCsus, CDOM, and FDOM observed in Garajonay relative to the other eddies.

Along BGT1 (Figure 1B), a pair of recently formed, irregularly shaped eddies -Nublo (cyclonic, ~70 km) and Anaga (anticyclonic, ~45 km)- were identified, although they were only properly sampled during BGT2 (Figure 1C). Their respective sizes reflect those of the islands responsible for their formation: Gran Canaria (~50 km) and the southern half of Tenerife (~45 km). Furthermore, their close proximity to the islands suggests that they developed recently. At these early stages, eddies exhibit intensified vertical pumping, in contrast to what is typically expected at more advanced stages of the eddy life cycle (McGillicuddy, 2016; Sangrà et al., 2007). This process results in the shoaling of density surfaces in cyclonic and intrathermocline eddies, lifting nutrients into the euphotic zone, while in anticyclones, isopycnals are deepened, effectively displacing nutrient-depleted waters from the well-illuminated surface layers (McGillicuddy, 2016). Such behavior has been documented previously in Canary Islands eddies during their early stages of development (Arístegui et al., 1997; Sangrà et al., 2009).

In Nublo, this dynamic is evidenced by the doming of the pycnocline, resulting in nutrient upwelling into the euphotic zone and is typically associated with enhanced primary production (Arístegui and Montero, 2005; Sangrà et al., 2009). In contrast, Anaga displayed a deepening of isopycnals (Arístegui et al., 1997; Hernández-Hernández et al., 2020), leading to nutrient downwelling, which usually results in reduced primary productivity (Sangrà et al., 2009) and increased water column respiration (Arístegui and Montero, 2005).

The submesoscale activity observed in the Nublo-Anaga eddy pair likely arises from two main factors: (1) their recent formation, which leads to ageostrophic imbalance and can trigger ageostrophic secondary circulations (Arístegui et al., 1997; Lévy et al., 2018; McGillicuddy, 2016), and (2) the direct interaction between the cyclonic and anticyclonic eddies (Chen et al., 2021). This activity is particularly pronounced within the frontal zone (Stns 29-31), where intense submesoscale dynamics appear to be driven by sharp lateral density gradients (Supplementary Figure S4B). These gradients result from the convergence of cold, fresher waters from Nublo with warmer, saltier waters from Anaga (Figures 2A, B; S5A, B). Such frontal interactions are known to play a significantly role in modulating the biological pump by enhancing vertical transport processes (Hernández-Hernández et al., 2020).

During eIMPACT-2, a five-month-old anticyclonic eddy was sampled approximately 560 km southwest of the Canary Islands (25.5°N, 19°W; Figure 1D), with an estimated diameter of ~180 km (Supplementary Figure S2B). This makes Bentayga one of the largest eddies observed in the region, exceeding the typical mesoscale eddy size range of 50–150 km (Chelton et al., 2011) and nearly doubling the size of only other intrathermocline eddy previously described in the Canary Eddy Corridor (the "PUMP" eddy, 4 months old and 92 km in diameter; Barceló-Llull et al., 2017).

Bentayga displayed the characteristic vertical structure of an intrathermocline eddy, with uplifted isopycnals in the upper layers and depressed isopycnals at depth. It also featured a low-salinity halostad core (Figure 2B) embedded within a well-defined pycnostad (density gradient) layer. Within this structure, both an upward intrusion of cooler, fresher water into the core and a downward transport of warmer, saltier water were observed -features that are consistent with classic intrathermocline eddy dynamics (Supplementary Figures S5A, B; Barceló-Llull et al., 2017; McGillicuddy, 2015, 2016; McGillicuddy et al., 2007; Valencia et al., 2025).

## 4.2 The influence of eddies on chlorophyll distribution

Cyclonic eddies in their early life stages, like Garajonay and Nublo, have important biological consequences through their upwelling effect, which enhances primary production by transporting nutrients into the euphotic zone (Arístegui et al., 1997). In the Canary region, the base of the euphotic zone generally coincides with the DCM and has been reported to range from ~50 m (Hernández-Hernández et al., 2020) to ~75–100 m (Arístegui et al., 1997), reflecting local variations in light penetration and DCM depth.

The DCM in Garajonay was unusually shallow and exceptionally productive. FChl-*a* peaked at 15 dbar at the eddy center (10.84 μg $L^{-1}$; Figure 2C), exceeding values reported for the NW African coastal upwelling system (Arístegui et al., 2004). Mean FChl-*a* around the DCM (± 5 dbar) at Garajonay stations (Stn 17-19) was 4.06 ± 0.35 μg $L^{-1}$, far above typical DCM concentrations in cyclonic eddies, which generally remain below 2 μg $L^{-1}$ (Bibby et al., 2008; Falkowski et al., 1991; Devresse et al., 2023; Jiao et al., 2014; Wang et al., 2017; Noyon et al., 2019).

Similarly, the DCMs of Nublo and Anaga inferred from FChl-*a* (67 and 87 dbar, respectively) were shallower than those reported in Hawaiian eddy pairs, where DCMs typically occur between ~103 and 145 m (Hawco et al., 2021; Barone et al., 2022). Mean FChl-*a*

around the DCM in Nublo (0.86 ± 0.05 μg $L^{-1}$) and Anaga (0.43 ± 0.02 μg $L^{-1}$) reflects the common pattern of higher Chl-*a* in cyclonic than anticyclonic eddies (Dufois et al., 2016) and exceeds values reported in other regions (Lasternas et al., 2013; Hawco et al., 2021). In contrast, Arístegui and Montero (2005) observed similar or higher DCM Chl-*a* in an anticyclonic eddy in the Canary Islands, attributed to entrainment of Chl-*a*-rich waters from a coastal filament off NW Africa.

The DCM in Bentayga, in contrast, showed lower mean FChl-*a* (0.27 ± 0.02 μg $L^{-1}$; Supplementary Figure S6A), consistent with other anticyclonic eddies near the Canary Islands (Arístegui and Montero, 2005; Lasternas et al., 2013). Within Bentayga, intra-eddy variability was evident, with the highest Chl-*a* at the outer ring and lowest at the inner ring, reflecting a spatial heterogeneity also observed in the Gulf of Alaska, Southern Ocean, Mozambique Channel, and eastern tropical South Pacific (McGillicuddy, 2016; Callbeck et al., 2017).

## 4.3 Impact of eddies on organic matter distribution and lability

Garajonay exhibited an enrichment in DOC at its center above the pycnocline, in contrast to the DOC depletion reported at the Brava Island eddy center of the Cape Verde Archipelago (Devresse et al., 2023). Moreover, POCsus increased by an order of magnitude relative to surrounding waters, exceeding previously reported values for Canary Islands eddies (Alonso-González et al., 2010a). Taken together, these observations indicate substantial organic matter production, and its subsequent accumulation and redistribution within the Garajonay eddy.

The recently formed eddy pair Nublo-Anaga acted as a two-way biological pump, a concept introduced by Arístegui and Montero (2005) to describe the coupled behavior of cyclonic and anticyclonic eddies generated downstream of Gran Canaria Island. This concept captures the dual role of mesoscale eddies in the oceanic carbon cycle. Cyclonic eddies, such as Nublo, enhance organic carbon export by promoting the upwelling of nutrient-rich waters, which stimulates phytoplankton production and increases the downward flux of organic matter. In contrast, anticyclonic eddies like Anaga can trap and subduct organic material, including both POCsus and DOC, into deeper ocean layers. Together, these processes illustrate the two-way exchange -downward export and upward recycling- highlighting the complex influence of eddies on carbon sequestration and nutrient cycling.

Further supporting this dual role, distinct plume-like structures of elevated DOC concentrations around the Nublo-Anaga eddy pair are consistent with observations from other regions. Similar enrichments of meso- and bathy-pelagic DOC have been reported in other Canary Islands eddies (Arístegui et al., 2003), in the Cape Verde Frontal Zone (Campanero et al., 2022), and in the northeastern Pacific Ocean (Lopez et al., 2020). In the Pacific, the DOC inputs were attributed to intense phytoplankton blooms and high abundances of gelatinous zooplankton, which increased the vertical export of organic carbon from the surface to deeper layers. In contrast, in the Cape Verde Frontal Zone, DOC accumulation was linked to intense meso- and submesoscale dynamics, which likely facilitated the observed export of DOC toward the mesopelagic layers, as also seen in our study.

The DOC distribution in Bentayga (Figure 4A; Supplementary Figure S8A), also presented plume-like structures of elevated concentration, likely resulting from intra-ring dynamics. This mesoscale variability may explain the significantly lower DOC concentrations measured in the eddy core below the pycnocline.

Regarding the optical properties of organic matter, the marine humic-like Peak M fluorescence, a byproduct of microbial respiration and organic matter remineralization, was typically depleted in surface waters due to photodegradation (Jørgensen et al., 2011; Omori et al., 2020). Owing to its persistence in the dark ocean, Peak M is considered part of the bio-refractory DOC pool and a reliable tracer of vertical transport processes, including eddy-driven upwelling and downwelling (Nieto-Cid et al., 2006; Lønborg and Álvarez-Salgado, 2014; Catalá et al., 2015b; Devresse et al., 2023). Conversely, the protein (tryptophan)-like Peak T, mainly produced by phytoplankton and heterotrophic bacteria, represents the labile or semi-labile DOC fraction and is thus a good indicator of recently produced DOM and dissolved organic nitrogen (Yamashita and Tanoue, 2003; Lønborg et al., 2015; Devresse et al., 2023).

When compared with methodologically equivalent studies, Peak M intensities observed in our eddies fall within the range reported by Martínez-Pérez et al. (2019) for the Mediterranean Sea (2-11 × $10^{-3}$ RU) and are consistent with values reported by De La Fuente et al. (2014), who found surface F(340/440) (similar to our Peak M) intensities of approximately 5-7 × $10^{-3}$ RU in the equatorial Atlantic Ocean. In contrast, our values were lower than those reported by Campanero et al. (2022) in the Cape Verde Frontal Zone, where Peak M ranged from 10.2 to 11.7 × $10^{-3}$ RU above the pycnocline and from 16.3 to 16.6 × $10^{-3}$ RU below it. Conversely, Peak M intensities in our study exceeded those observed in the Northeast Atlantic by Lønborg and Álvarez-Salgado (2014), who reported a bulk surface Peak M value of 0.45 ± 0.22 QSU (quinine sulfate units, equivalent to 6.8 ± 3.3 × $10^{-3}$ RU). Similar comparison can be made with protein-like Peak T. In the Cape Verde Frontal Zone, Peak T ranged from 14.8 to 17.2 × $10^{-3}$ RU above the pycnocline and from 10.9 to 11.7 × $10^{-3}$ RU below it (Campanero et al., 2022). In the Northeast Atlantic Ocean, Lønborg and Álvarez-Salgado (2014) reported an average Peak T concentration of 1.07 ± 0.42 QSU (equivalent to 16.1 ± 6.3 $10^{-3}$ RU), while Martínez-Pérez et al. (2019) reported Peak T values between 2 and 15 × $10^{-3}$ RU in the Mediterranean Sea. While peak M and peak T usually vary opposite with depth, within Garajonay both peaks exhibited spatial distributions and concentration patterns similar to chlorophyll *a*, suggesting enhanced DOC production and remineralization.

Lønborg and Álvarez-Salgado (2014) suggested that absorbance at 254 nm can be used as an optical proxy for DOC. The direct ordinary distance regression between DOC and $a_{CDOM}(254)$ in epipelagic and mesopelagic waters was highly significant (DOC = 49.6 (± 1.3) $a_{CDOM}(254)$ + 5 (± 1.4); $R^2$ = 0.71; $p$ < 0.001; n = 583). This strong relationship indicates that variability in $a_{CDOM}(254)$ closely mirrors that of DOC. Accordingly, given their tight coupling, we did not further

elaborate on $a_{CDOM}(254)$ variability, as it does not provide additional independent information beyond that already captured by DOC.

The absorption coefficient of $a_{CDOM}(320)$, is typically low in surface waters due to photodegradation (Catalá et al., 2015a; Nelson et al., 2004; Nelson and Siegel, 2013). In Garajonay, slightly elevated $a_{CDOM}(320)$ was observed above the pycnocline (Supplementary Figure S9B), similar to patterns reported by Campanero et al. (2022) in the Cape Verde Frontal Zone, where waters influenced by multiple eddies exhibited enhanced surface $a_{CDOM}(320)$, indicating that *in situ* production and/or external inputs outweighed photodegradation. Garajonay values are consistent with $a_{CDOM}(325)$ (0.12 to 0.26 $m^{-1}$) reported by Devresse et al. (2023) in the Brava Island eddy, although the pronounced central maximum seen there was not evident. By contrast, Wang et al. (2017) reported $a_{CDOM}(350)$ of 0.241 $m^{-1}$ at the eddy edge and 0.161 $m^{-1}$ at the center of two cyclonic eddies in the South China Sea.

In Nublo, average $a_{CDOM}(320)$ above and below the pycnocline was 0.20 $m^{-1}$, within the $a_{CDOM}(325)$ range reported for the Brava Island eddy by Devresse et al. (2023). Similar to Garajonay, Nublo exhibited elevated surface $a_{CDOM}(320)$, particularly along the edges (Supplementary Figure S9B), suggesting that, as in the Cape Verde Frontal Zone (Campanero et al., 2022), *in situ* production and/or external inputs likely exceed photodegradation.

No studies have explicitly examined CDOM or FDOM dynamics within intrathermocline eddies, representing a critical gap in understanding their role in organic matter cycling. In Bentayga, horizontal FDOM variability likely reflects mesoscale intrathermocline dynamics: upward transport of nutrient- and humic-like DOM-rich deep waters increases refractory peak M concentrations toward the eddy periphery, while nutrient enrichment stimulates primary production and microbial degradation of fresh organic matter (peak T), further contributing to humic-like DOM accumulation. This interpretation is supported by observed temperature and salinity gradients from the center to the periphery (Supplementary Figures S5A, B; Table 1).

## 4.4 Local production and consumption of organic matter in island-induced eddies

The variability of AOU below the pycnocline was primarily driven by water mass mixing, physical motion processes and large-scale remineralization processes occurring from the water mass formation areas to the CEC, consistent with patterns observed in the Eastern North Atlantic (Campanero et al., 2022; Lønborg and Álvarez-Salgado, 2014). Water masses present in the Canary region includes Eastern North Atlantic Central Water, Antarctic Intermediate Water, Mediterranean Water, and Labrador Sea Water (Lønborg and Álvarez-Salgado, 2014; Pastor et al., 2015; Pérez et al., 1995). This variability is captured by a multiple linear regression of AOU with S, θ, $S^2$ and $\theta^2$ ($R^2 = 0.96$), that is equivalent to a multiple linear regression with the water mass proportions obtained with an optimum multiparameter analyses (De La Fuente et al., 2014). Despite the high proportion of AOU variability explained by water mass mixing, physical motion and large-scale biogeochemical processes, the standard error of the estimate remains an order of magnitude greater than the measurement error (~1 μmol $kg^{-1}$), indicating that local biogeochemical processes also significantly shape AOU distributions. In particular, positive ΔAOU, indicative of local oxygen consumption, extends to greater depths in the one-month-old cyclonic eddy Garajonay and in the five-month-old anticyclonic eddy Bentayga. This pattern likely reflects the cumulative effects of organic matter export and remineralization over the lifetime of each eddy, as deeper layers have been exposed for longer to the breakdown of both dissolved and particulate organic carbon.

At the local scale, approximately 68 ± 15% of the oxygen demand -assuming a Redfieldian -$O_2$/Corg stoichiometric ratio of 1.36 mol $O_2$ mol $C^{-1}$ (Anderson and Sarmiento, 1994)- is supported by DOC remineralization. This contribution is substantially higher than reported for the Sargasso Sea (15-41%; Hansell and Carlson, 2001), South Pacific Ocean (21-47%), Indian Ocean (18-43%; Doval and Hansell, 2000), Eastern Subtropical North Pacific (30%; Abell et al., 2000), Cape Verde Frontal Zone (21%; Campanero et al., 2022) and Red Sea (21%; Calleja et al., 2019), and closely resembles that observed in the eastern basin of the Mediterranean Sea (66 ± 10%; Catalá et al., 2018). Catalá et al. (2018) attributed this high DOC contribution to seasonal accumulation and subsequent export from surface layers (<50 dbar) to the winter mixed layer (<150 dbar), but this mechanism does not appear to dominate in our study.

POCsus, assuming Redfield stoichiometry, accounts for 20 ± 1% of the local oxygen demand. Combined with DOC, these pools contribute up to 88% (68 + 20%) of total local oxygen consumption, indicating that sinking POC plays a relatively minor role in carbon remineralization. This pattern aligns with previous observations in the Canary Current region (Alonso-González et al., 2009, 2010a; Santana-Falcón et al., 2017) but is only valid for the months surveyed, as POC fluxes show pronounced spatio-temporal variability.

The prominence of POCsus over sinking POC reflects its origin: small "suspended" particles may result from disaggregation of sinking particles by microbial and zooplankton activity, self-assembly of DOM into microgels, or physical processes (Alonso-González et al., 2010b). Sediment trap data south of Gran Canaria over 1.5 years showed that in summer and autumn, 62% of POC flux was slowly sinking particles (0.7–11 m $d^{-1}$), while in winter and spring, large, rapidly sinking particles (>326 m $d^{-1}$), dominated (53% of the flux) (Alonso-González et al., 2010a). Notably, the combined DOC and POCsus contribution in our study exceeded the contribution reported in other oceanic regions. For example, in the Cape Verde Frontal Zone, DOC and POCsus together accounted for only 23.6% of oxygen demand (Campanero et al., 2022), highlighting the distinctive role of these carbon pools in different regions.

Water mass mixing, physical motion and large-scale biogeochemical processes explained 89% of the variability in $a_{CDOM}(254)$ but only 5% in $a_{CDOM}(320)$. Including AOU in the multiple regression reduced the SE for $a_{CDOM}(254)$, which nevertheless remained 2.5 times higher than the measurement error (0.02 $m^{-1}$). In contrast, the SE for $a_{CDOM}(320)$ was nearly

equal to the measurement error. This absence of correlation aligns with Nelson & Siegel (2013), who found a significant AOU- $a_{CDOM}$ (325) relationship in the Pacific and Indian Oceans, but not in the Atlantic, and with Stedmon and Nelson (2015), who attributed it to rapid mixing of high-CDOM, low-AOU waters, and slow accumulation of CDOM in subsurface water masses.

For $a_{CDOM}(254)$, a significant negative slope with AOU (-0.0051 ± 0.0005 $m^{-1}$ (μmol kg)$^{-1}$) indicated net consumption of $a_{CDOM}$ (254) with increasing oxygen demand. This slope is consistent with values reported by Catalá et al. (2018) in the Mediterranean Sea (-0.0048 ± 0.0004 $m^{-1}$ kg $\mu mol^{-1}$), but contrasts with findings from Campanero et al. (2022), who observed a positive relationship (0.0023 ± 0.0009 $m^{-1}$ kg $\mu mol^{-1}$) in the Cape Verde Frontal Zone, suggesting net $a_{CDOM}(254)$ production in that area.

As much as 86% of the variability in Peak M and 53% of the variability in Peak T was explained by water mass mixing, physical motion and large-scale biogeochemical processes. The inclusion of AOU significantly improved the explained variance for both optical properties, suggesting that local remineralization processes contribute to the net production of Peak M and the net consumption of Peak T in the ocean interior. As discussed below, this interpretation is supported by the significant relationships observed between Peak M and Peak T and AOU.

The Peak ΔM/ΔAOU slope of 9.9 ± 1.0 $\times 10^{-5}$ RU $kg^{-1}$ μmol obtained in this study exceeded comparable regional estimates. While several studies have examined the positive relationship between humic-like fluorescence and AOU (e.g., Xiao et al., 2023; Wang et al., 2017), we focus here on methodologically comparable studies that reported ΔM/ΔAOU slopes. In the equatorial Atlantic, De La Fuente et al. (2014) obtained a slope of 3.1 ± 0.1 $\times 10^{-5}$ RU $\mu mol^{-1}$ kg at depths below 200 m, using residuals of AOU and F (340/440) (similar to our Peak M). In the Mediterranean Sea, Martínez-Pérez et al. (2019) found a Peak ΔM/ΔAOU slope of 5.0 ± 1.0 $\times 10^{-5}$ RU $\mu mol^{-1}$ kg for the ultraoligotrophic eastern basin and 1.6 ± 0.4 $\times 10^{-5}$ RU $\mu mol^{-1}$ kg for the western basin, and in the Cape Verde Frontal Zone, Campanero et al. (2022) reported a slope of 1.8 ± 0.7 $\times 10^{-5}$ RU $\mu mol^{-1}$ kg.

In contrast, the Peak ΔT/ΔAOU slope indicates that Peak T is primarily generated in surface waters and subsequently removed in the ocean interior (Catalá et al., 2015b; Campanero et al., 2022; Jørgensen et al., 2011). Peak ΔT/ΔAOU slope (-11.1 ± 1.3 × $10^{-5}$ RU $kg^{-1}$ μmol) is also higher than methodologically comparable studies in the Western Mediterranean (-2.7 ± 1.2 $\times 10^{-5}$ RU $\mu mol^{-1}$ kg), but comparable in magnitude to the ultra-oligotrophic Eastern Mediterranean Basin (-8.0 ± 3.0 $\times 10^{-5}$ RU $\mu mol^{-1}$ kg; Martínez-Pérez et al., 2019).

## 5 Conclusions

High-resolution surveys underscore the critical role of mesoscale and submesoscale structures in regulating organic matter distribution and cycling within the eddy field downstream of the Canary Islands. Four distinct eddies were characterized: (1) Garajonay, a cyclonic eddy confined by two anticyclonic structures and two islands, which provided optimal conditions for the development of phytoplankton blooms; (2) Nublo and Anaga, a developing cyclonic-anticyclonic eddy pair formed downstream of the islands, acting as a two-way biological pump; and (3) Bentayga, an exceptionally large anticyclonic intrathermocline eddy drifting along the CEC toward the subtropical gyre.

At the mesoscale, biogeochemical variability was strongly influenced by both eddy lifespan and polarity. Lifespan-based comparisons revealed that the developing cyclonic eddy Nublo exhibited higher concentrations of DOC, $a_{CDOM}(254)$, $a_{CDOM}(320)$, and Peak T below the pycnocline, as well as elevated $a_{CDOM}(254)$ above it, compared to the more mature cyclonic eddy Garajonay. These differences suggest a progressive loss of DOM components as cyclonic eddies age. Among anticyclonic eddies, Bentayga consistently exhibited higher Peak M values than Anaga, indicating an enrichment in humic-like material with anticyclonic eddy aging.

When eddy polarity was considered, clear differences were also evident. Above the pycnocline, Nublo showed higher DOC, POCsus, and $a_{CDOM}(320)$ than the anticyclonic Anaga. Similarly, Garajonay displayed higher $a_{CDOM}(320)$ and Peak T levels than the mature Bentayga. Below the pycnocline, Nublo had greater Peak M fluorescence than Anaga, whereas Garajonay exhibited lower DOC, $a_{CDOM}(254)$, $a_{CDOM}(320)$, and Peak T compared to Bentayga. These findings reveal a strong dependence of the optical properties of organic matter dynamics on eddy polarity.

Submesoscale motions were evident at the Nublo-Anaga front, marked by differences in DOC concentrations above the pycnocline and Peak M fluorescence below. In Bentayga, spatial variability was observed across concentric rings, with DOC, $a_{CDOM}(254)$, and Peak M differing above the pycnocline, while below it only Peak M showed significant variation in the outer ring. These patterns highlight the central role of DOM -particularly its optical components- in driving submesoscale biogeochemical variability.

This study provides the first regional assessment of local remineralization processes affecting organic matter within the Canary region, showing that the cycling of DOC, CDOM and FDOM is significantly influenced by both mesoscale and submesoscale dynamics. Significant regression coefficients between AOU and DOC, POCsus, $a_{CDOM}(254)$, Peak M, and Peak T indicate intense local consumption of DOC and POCsus, as well as active transformation of fluorescent components -specifically the removal of Peak T and accumulation of Peak M- relative to other oceanic systems.

Notably, the slopes of the DOC/AOU and POCsus/AOU relationships suggest, that during the surveyed months, the 88% of the oxygen demand in the mesopelagic CEC can be explained by the remineralization of DOC and suspended POC, implying that sinking POM plays only a minor role in carbon remineralization in the Canary region during our time of study.

## Data availability statement

The raw data supporting the conclusions of this article will be made available by the authors, without undue reservation.

## Author contributions

JLG: Data curation, Data analysis, Writing – original draft, Investigation. JA: Conceptualization, Resources, Supervision, Validation, Writing – original draft, Investigation. MJP: Data curation, Writing – review & editing, Investigation. VV: Data curation, Writing – review & editing, Investigation. NH-H: Data curation, Writing – review & editing, Investigation. MN-C: Data curation, Writing – review & editing, Investigation. MG-C: Data curation, Writing – review & editing, Investigation. AM-M: Data curation, Writing – review & editing, Investigation. XÁ-S: Conceptualization, Resources, Supervision, Validation, Writing – original draft, Investigation.

## Funding

The author(s) declared that financial support was received for this work and/or its publication. This research was funded by the e-IMPACT project (PID2019-109084RB-C21 and -C22) from JA and XA-S, supported by MCIN/AEI/10.13039/501100011033. XA-S and JA were also supported by the OceanICU project (HORIZON-CL6-2022-CLIMATE-01-02). This work was funded by the European Union under grant agreement no. 101083922 (OceanICU) and UK Research. JG was supported by a predoctoral fellowships from the Spanish Ministry of Science, Innovation and Universities (PRE2020-095806).

## Acknowledgments

We would like to thank the captain and crew of the R/V Sarmiento de Gamboa, the technicians of the Unidad de Tecnologıa Marina (UTM-CSIC) and the scientists onboard for their valuable help during the eIMPACT-1 and eIMPACT-2 cruises. We also acknowledge the use of imagery from the NASA Worldview application (https://worldview.earthdata.nasa.gov), part of NASA's Earth Science Data and Information System (ESDIS).

## Conflict of interest

The authors declared that this work was conducted in the absence of any commercial or financial relationships that could be construed as a potential conflict of interest.

The authors JA, XÁ-S declared that they were an editorial board member of Frontiers, at the time of submission. This had no impact on the peer review process and the final decision.

## Generative AI statement

The author(s) declared that generative AI was not used in the creation of this manuscript.

Any alternative text (alt text) provided alongside figures in this article has been generated by Frontiers with the support of artificial intelligence and reasonable efforts have been made to ensure accuracy, including review by the authors wherever possible. If you identify any issues, please contact us.

## Publisher's note



## Author disclaimer

Views and opinions expressed are however those of the author (s) only and do not necessarily reflect those of the European Union or European Research Executive Agency. Neither the European Union nor the granting authority can be held responsible for them.

## Supplementary material

The Supplementary Material for this article can be found online at: https://www.frontiersin.org/articles/10.3389/fmars.2026.1711689/full#supplementary-material

## References

Abell, J., Emerson, S., and Renaud, P. (2000). Distributions of TOP, TON and TOC in the North Pacific Subtropical Gyre: Implications for nutrient supply in the surface ocean and remineralization in the upper thermocline. *J. Mar. Res.* 58, 203–222. doi: 10.1357/002224000321511142

Alonso-González, I. J., Arístegui, J., Lee, C., and Calafat, A. (2010a). Regional and temporal variability of sinking organic matter in the subtropical northeast Atlantic Ocean: a biomarker diagnosis. *Biogeosciences* 7, 2101–2115. doi: 10.5194/bg-7-2101-2010

Alonso-González, I. J., Arístegui, J., Lee, C., Sanchez-Vidal, A., Calafat, A., Fabrés, J., et al. (2010b). Role of slowly settling particles in the ocean carbon cycle. *Geophys. Res. Lett.* 37, L13608. doi: 10.1029/2010GL043827

Alonso-González, I. J., Arístegui, J., Vilas, J. C., and Hernández-Guerra, A. (2009). Lateral POC transport and consumption in surface and deep waters of the Canary Current region: A box model study. *Global Biogeochem. Cycles* 23, GB2007. doi: 10.1029/2008GB003185

Álvarez-Salgado, X. A., Nieto-Cid, M., Álvarez, M., Pérez, F. F., Morin, P., and Mercier, H. (2013). New insights on the mineralization of dissolved organic matter in central, intermediate, and deep water masses of the northeast North Atlantic. *Limnol. Oceanogr.* 58, 681–696. doi: 10.4319/lo.2013.58.2.0681

Álvarez-Salgado, X. A., and Arístegui, J. (2015). "Organic matter dynamics in the Canary Current," in *Oceanographic and biological features in the Canary Current Large Marine Ecosystem*. Eds. L. Valdés and I. Déniz-GonzálezIOC Technical Series, No. 115 (IOC-UNESCO, Paris), 151–159. Available online at: http://hdl.handle.net/1834/9185 (Accessed Feburuary 9, 2026).

Anderson, L. A., and Sarmiento, J. L. (1994). Redfield ratios of remineralization determined by nutrient data analysis. *Global Biogeochem. Cycles* 8, 65–80. doi: 10.1029/93GB03318

Arístegui, J., Barton, E. D., Montero, M. F., García-Muñoz, M., and Escánez, J. (2003). Organic carbon distribution and water column respiration in the NW Africa-Canaries Coastal Transition Zone. *Aquat. Microb. Ecol.* 33, 289–301. doi: 10.3354/ame033289

Arístegui, J., Barton, E. D., Tett, P., Montero, M. F., García-Muñoz, M., and Basterretxea, G. (2004). Variability in plankton community structure, metabolism, and vertical carbon fluxes along an upwelling filament (Cape Juby, NW Africa). *Prog. Oceanogr.* 62, 95–113. doi: 10.1016/j.pocean.2004.07.004

Arístegui, J., and Montero, M. F. (2005). Temporal and spatial changes in plankton respiration and biomass in the Canary Islands region: the effect of mesoscale variability. *J. Mar. Syst.* 54, 65–82. doi: 10.1016/j.jmarsys.2004.07.004

Arístegui, J., Sangrá, P., Hernández-León, S., Cantón, M., Hernández-Guerra, A., and Kerling, J. L. (1994). Island-induced eddies in the Canary islands. *Deep Sea Res. Part I: Oceanogr. Res. Papers* 41, 1509–1525. doi: 10.1016/0967-0637(94)90058-2

Arístegui, J., Tett, P., Hernández-Guerra, A., Basterretxea, G., Montero, M. F., Wild, K., et al. (1997). The influence of island-generated eddies on chlorophyll distribution: a study of mesoscale variation around Gran Canaria. *Deep Sea Res. Part I: Oceanogr. Res. Papers* 44, 71–96. doi: 10.1016/S0967-0637(96)00093-3

Baltar, F., Arístegui, J., Montero, M. F., Espino, M., Gasol, J. M., and Herndl, G. J. (2009). Mesoscale variability modulates seasonal changes in the trophic structure of nano- and picoplankton communities across the NW Africa-Canary Islands transition zone. *Prog. Oceanogr.* 83, 180–188. doi: 10.1016/j.pocean.2009.07.016

Barceló-Llull, B., Sangrà, P., Pallàs-Sanz, E., Barton, E. D., Estrada-Allis, S. N., Martínez-Marrero, A., et al. (2017). Anatomy of a subtropical intrathermocline eddy. *Deep Sea Res. Part I: Oceanogr. Res. Papers* 124, 126–139. doi: 10.1016/j.dsr.2017.03.012

Barone, B., Church, M. J., Dugenne, M., Hawco, N. J., Jahn, O., White, A. E., et al. (2022). Biogeochemical dynamics in adjacent mesoscale eddies of opposite polarity. *Global Biogeochem. Cycles* 36, e2021GB007115–e2021GB007115. doi: 10.1029/2021GB007115

Barton, E. D., and Arístegui, J. (2004). The Canary Islands coastal transition zone – upwelling, eddies and filaments. *Prog. Oceanogr.* 62, 67–69. doi: 10.1016/j.pocean.2004.08.003

Barton, E. D., Arıstegui, J., Tett, P., Cantón, M., Garcıa-Braun, J., Hernández-León, S., et al. (1998). The transition zone of the Canary Current upwelling region. *Prog. Oceanogr.* 41, 455–504. doi: 10.1016/S0079-6611(98)00023-8

Belkin, N., Guy-Haim, T., Rubin-Blum, M., Lazar, A., Sisma-Ventura, G., Kiko, R., et al. (2022). Influence of cyclonic and anticyclonic eddies on plankton in the southeastern Mediterranean Sea during late summertime. *Ocean Sci.* 18, 693–715. doi: 10.5194/os-18-693-2022

Benson, B. B., and Krause, D.Jr. (1984). The concentration and isotopic fractionation of oxygen dissolved in freshwater and seawater in equilibrium with the atmosphere. *Limnol. Oceanogr.* 29, 620–632. doi: 10.4319/lo.1984.29.3.0620

Bibby, T. S., Gorbunov, M. Y., Wyman, K. W., and Falkowski, P. G. (2008). Photosynthetic community responses to upwelling in mesoscale eddies in the subtropical North Atlantic and Pacific Oceans. *Deep Sea Res. Part II: Topical Stud. Oceanogr.* 55, 1310–1320. doi: 10.1016/j.dsr2.2008.01.014

Bonan, G. B., and Doney, S. C. (2018). Climate, ecosystems, and planetary futures: The challenge to predict life in Earth system models. *Science* 359, eaam8328–eaam8328. doi: 10.1126/science.aam8328

Boyd, P. W., Claustre, H., Levy, M., Siegel, D. A., and Weber, T. (2019). Multi-faceted particle pumps drive carbon sequestration in the ocean. *Nature* 568, 327–335. doi: 10.1038/s41586-019-1098-2

Brannigan, L., Marshall, D. P., Garabato, A. C. N., Nurser, A. J. G., and Kaiser, J. (2017). Submesoscale instabilities in mesoscale eddies. *J. Phys. Oceanogr.* 47, 3061–3085. doi: 10.1175/JPO-D-16-0178.1

Callbeck, C. M., Lavik, G., Stramma, L., Kuypers, M. M. M., and Bristow, L. A. (2017). Enhanced Nitrogen Loss by Eddy-Induced Vertical Transport in the Offshore Peruvian Oxygen Minimum Zone. *PLOS ONE* 12, e0170059. doi: 10.1371/journal.pone.0170059

Calleja, M. L., Al-Otaibi, N., and Morán, X. A. G. (2019). Dissolved organic carbon contribution to oxygen respiration in the central Red Sea. *Sci. Rep.* 9, 4690–4690. doi: 10.1038/s41598-019-40753-w

Campanero, R., Burgoa, N., Fernández-Castro, B., Valiente, S., Nieto-Cid, M., Martínez-Pérez, A. M., et al. (2022). High-resolution variability of dissolved and suspended organic matter in the Cape Verde Frontal Zone. *Front. Mar. Sci.* 9. doi: 10.3389/fmars.2022.1006432

Cardoso, C., Caldeira, R. M. A., Relvas, P., and Stegner, A. (2020). Islands as eddy transformation and generation hotspots: Cabo Verde case study. *Prog. Oceanogr.* 184, 102271–102271. doi: 10.1016/j.pocean.2020.102271

Catalá, T. S., Martínez-Pérez, A. M., Nieto-Cid, M., Álvarez, M., Otero, J., Emelianov, M., et al. (2018). Dissolved Organic Matter (DOM) in the open Mediterranean Sea. I. Basin–wide distribution and drivers of chromophoric DOM. *Prog. Oceanogr.* 165, 35–51. doi: 10.1016/j.pocean.2018.05.002

Catalá, T. S., Reche, I., Álvarez, M., Khatiwala, S., Guallart, E. F., Benítez-Barrios, V. M., et al. (2015a). Water mass age and aging driving chromophoric dissolved organic matter in the dark global ocean. *Global Biogeochem. Cycles* 29, 917–934. doi: 10.1002/2014GB005048

Catalá, T. S., Reche, I., Fuentes-Lema, A., Romera-Castillo, C., Nieto-Cid, M., Ortega-Retuerta, E., et al. (2015b). Turnover time of fluorescent dissolved organic matter in the dark global ocean. *Nat. Commun.* 6, 5986–5986. doi: 10.1038/ncomms6986

Cerdán-García, E., Alvarez-Salgado, X. A., Aristegui, J., Martinez-Marrero, A., and Benavides, M. (2024). *Eddy-driven diazotroph distribution: horizontal variability prevails over particle sinking speed*. (London, UK: Nature Publishing Group). doi: 10.21203/rs.3.rs-3953856/v1

Chelton, D. B., deSzoeke, R. A., Schlax, M. G., Naggar, K. E., and Siwertz, N. (1998). Geographical variability of the first baroclinic rossby radius of deformation. *J. Phys. Oceanogr.* 28, 433–460. doi: 10.1175/15200485(1998)028%3C0433:GVOTFB%3E2.0.CO;2

Chelton, D. B., Schlax, M. G., and Samelson, R. M. (2011). Global observations of nonlinear mesoscale eddies. *Prog. Oceanogr.* 91, 167–216. doi: 10.1016/j.pocean.2011.01.002

Chen, X., Schallenberg, C., Phillips, H., and Chase, Z. (2021). Biogeochemical characteristics of eddies in the East Australian Current depend on eddy type, history and location. *J. Mar. Syst.* 216, 103512–103512. doi: 10.1016/j.jmarsys.2021.103512

Coble, P. G. (1996). Characterization of marine and terrestrial DOM in seawater using excitation-emission matrix spectroscopy. *Mar. Chem.* 51, 325–346. doi: 10.1016/0304-4203(95)00062-3

De La Fuente, P., Marrasé, C., Canepa, A., Antón Álvarez-Salgado, X., Gasser, M., Fajar, N. M., et al. (2014). Does a general relationship exist between fluorescent dissolved organic matter and microbial respiration?—The case of the dark equatorial Atlantic Ocean. *Deep Sea Res. Part I: Oceanogr. Res. Papers* 89, 44–55. doi: 10.1016/j.dsr.2014.03.007

Devresse, Q., Becker, K. W., Dilmahamod, A. F., Ortega-Retuerta, E., and Engel, A. (2023). Dissolved organic matter fluorescence as a tracer of upwelling and microbial activities in two cyclonic eddies in the eastern tropical north atlantic. *J. Geophys. Res.: Oceans* 128, e2023JC019821–e2023JC019821. doi: 10.1029/2023JC019821

Ding, X., Lü, H., Zhu, Y., Zhang, L., Zhou, Y., and Bai, L. (2024). A study of the cyclonic eddy shedding phenomenon in the Agulhas Return Current. *J. Sea Res.* 198, 102481–102481. doi: 10.1016/j.seares.2024.102481

Doval, M. D., and Hansell, D. A. (2000). Organic carbon and apparent oxygen utilization in the western South Pacific and the central Indian Oceans. *Mar. Chem.* 68, 249–264. doi: 10.1016/S0304-4203(99)00081-X

Ducklow, H. (2001). Upper ocean carbon export and the biological pump. *Oceanography* 14, 50–54. doi: 10.5670/oceanog.2001.06

Dufois, F., Hardman-Mountford, N. J., Greenwood, J., Richardson, A. J., Feng, M., and Matear, R. J. (2016). Anticyclonic eddies are more productive than cyclonic eddies in subtropical gyres because of winter mixing. *Sci. Adv.* 2, e1600282–e1600282. doi: 10.1126/sciadv.1600282

Falkowski, P. G., Ziemann, D., Kolber, Z., and Bienfang, P. K. (1991). Role of eddy pumping in enhancing primary production in the ocean. *Nature* 352, 55–58. doi: 10.1038/352055a0

Fofonoff, N., and Millard, R. (1983). Algorithms for computation of fundamental properties of seawater. *UNESCO Tech. Pap. Mar. Sci.* 44.

Hansell, D. A., and Carlson, C. A. (2001). Biogeochemistry of total organic carbon and nitrogen in the Sargasso Sea: control by convective overturn. *Deep Sea Res. Part II: Topical Stud. Oceanogr.* 48, 1649–1667. doi: 10.1016/S0967-0645(00)00153-3

Hansen, H. P., and Koroleff, F. (1999). "Determination of nutrients," in *Methods of seawater analysis* (Weinheim, Germany: John Wiley & Sons, Ltd), 159–228. doi: 10.1002/9783527613984.ch10

Hansen, A. M., Kraus, T. E. C., Pellerin, B. A., Fleck, J. A., Downing, B. D., and Bergamaschi, B. A. (2016). Optical properties of dissolved organic matter (DOM): Effects of biological and photolytic degradation. *Limnol. Oceanogr.* 61, 1015–1032. doi: 10.1002/lno.10270

Hawco, N. J., Barone, B., Church, M. J., Babcock-Adams, L., Repeta, D. J., Wear, E. K., et al. (2021). Iron depletion in the deep chlorophyll maximum: mesoscale eddies as natural iron fertilization experiments. *Global Biogeochem. Cycles* 35, e2021GB007112–e2021GB007112. doi: 10.1029/2021GB007112

Helms, J. R., Stubbins, A., Ritchie, J. D., Minor, E. C., Kieber, D. J., and Mopper, K. (2008). Absorption spectral slopes and slope ratios as indicators of molecular weight, source, and photobleaching of chromophoric dissolved organic matter. *Limnol. Oceanogr.* 53, 955–969. doi: 10.4319/lo.2008.53.3.0955

Hernández-Hernández, N., Arístegui, J., Montero, M. F., Velasco-Senovilla, E., Baltar, F., Marrero-Díaz, Á., et al. (2020). Drivers of plankton distribution across mesoscale eddies at submesoscale range. *Front. Mar. Sci.* 7. doi: 10.3389/fmars.2020.00667

Hernández-Hernández, N., Santana-Falcón, Y., Estrada-Allis, S., and Arístegui, J. (2021). Short-term spatiotemporal variability in picoplankton induced by a submesoscale front south of gran canaria (Canary islands). *Front. Mar. Sci.* 8. doi: 10.3389/fmars.2021.592703

IOC, SCOR and IAPSO (2010). *The international thermodynamic equation of seawater – 2010: Calculation and use of thermodynamic properties* (Paris: UNESCO (Intergovernmental Oceanographic Commission). Available online at: https://www.teos-10.org/pubs/TEOS-10_Manual.pdf (Accessed Feburuary 9, 2026).

Jiao, N., Zhang, Y., Zhou, K., Li, Q., Dai, M., Liu, J., et al. (2014). Revisiting the CO_2 "source" problem in upwelling areas – a comparative study on eddy upwellings in the South China Sea. *Biogeosciences* 11, 2465–2475. doi: 10.5194/bg-11-2465-2014

Jiménez, B., Sangrà, P., and Mason, E. (2008). A numerical study of the relative importance of wind and topographic forcing on oceanic eddy shedding by tall, deep water islands. *Ocean Model.* 22, 146–157. doi: 10.1016/j.ocemod.2008.02.004

Jørgensen, L., Stedmon, C. A., Kragh, T., Markager, S., Middelboe, M., and Søndergaard, M. (2011). Global trends in the fluorescence characteristics and distribution of marine dissolved organic matter. *Mar. Chem.* 126, 139–148. doi: 10.1016/j.marchem.2011.05.002

Kérouel, R., and Aminot, A. (1997). Fluorometric determination of ammonia in sea and estuarine waters by direct segmented flow analysis. *Mar. Chem.* 57, 265–275. doi: 10.1016/S0304-4203(97)00040-6

Langdon, C. (2010). *Determination of dissolved oxygen in seawater by Winkler titration using the amperometric technique*. Available online at: https://api.semanticscholar.org/CorpusID:197105685 (Accessed Feburuary 9, 2026).

Lasternas, S., Piedeleu, M., Sangrà, P., Duarte, C. M., and Agustí, S. (2013). Forcing of dissolved organic carbon release by phytoplankton by anticyclonic mesoscale eddies in the subtropical NE Atlantic Ocean. *Biogeosciences* 10, 2129–2143. doi: 10.5194/bg-10-2129-2013

Lévy, M., Franks, P. J. S., and Smith, K. S. (2018). The role of submesoscale currents in structuring marine ecosystems. *Nat. Commun.* 9, 4758–4758. doi: 10.1038/s41467-018-07059-3

Lønborg, C., and Álvarez-Salgado, X. A. (2014). Tracing dissolved organic matter cycling in the eastern boundary of the temperate North Atlantic using absorption and fluorescence spectroscopy. *Deep Sea Res. Part I: Oceanogr. Res. Papers* 85, 35–46. doi: 10.1016/j.dsr.2013.11.002

Lønborg, C., Yokokawa, T., Herndl, G. J., and Antón Álvarez-Salgado, X. (2015). Production and degradation of fluorescent dissolved organic matter in surface waters of the eastern north Atlantic ocean. *Deep-Sea Res. I: Oceanogr. Res. Pap.* 96, 28–37. doi: 10.1016/j.dsr.2014.11.001

Lopez, C. N., Robert, M., Galbraith, M., Bercovici, S. K., Orellana, M. V., and Hansell, D. A. (2020). High temporal variability of total organic carbon in the deep northeastern pacific. *Front. Earth Sci.* 8. doi: 10.3389/feart.2020.00080

Mahadevan, A., and Tandon, A. (2006). An analysis of mechanisms for submesoscale vertical motion at ocean fronts. *Ocean Modelling*14, 241–256. doi: 10.1016/j.ocemod.2006.05.006

Mahadevan, A. (2016). The impact of submesoscale physics on primary productivity of plankton. *Annu. Rev. Mar. Sci.* 8, 161–184. doi: 10.1146/annurev-marine-010814-015912

Maiti, K., Benitez-Nelson, C. R., Rii, Y., and Bidigare, R. (2008). The influence of a mature cyclonic eddy on particle export in the lee of Hawaii. *Deep Sea Res. Part II: Topical Stud. Oceanogr.* 55, 1445–1460. doi: 10.1016/j.dsr2.2008.02.008

Martínez-Pérez, A. M., Catalá, T. S., Nieto–Cid, M., Otero, J., Álvarez, M., Emelianov, M., et al. (2019). Dissolved organic matter (DOM) in the open Mediterranean Sea. II: Basin–wide distribution and drivers of fluorescent DOM. *Prog. Oceanogr.* 170, 93–106. doi: 10.1016/j.pocean.2018.10.019

McGillicuddy, D. J. (2015). Formation of intrathermocline lenses by eddy–wind interaction. *J. Phys. Oceanogr.* 45, 606–612. doi: 10.1175/JPO-D-14-0221.1

McGillicuddy, D. J. (2016). Mechanisms of physical-biological-biogeochemical interaction at the oceanic mesoscale. *Annu. Rev. Mar. Sci.* 8, 125–159. doi: 10.1146/annurev-marine-010814-015606

McGillicuddy, D. J., Anderson, L. A., Bates, N. R., Bibby, T., Buesseler, K. O., Carlson, C. A., et al. (2007). Eddy/wind interactions stimulate extraordinary mid-ocean plankton blooms. *Science* 316, 1021–1026. doi: 10.1126/science.1136256

McWilliams, J. C. (2008). "The nature and consequences of oceanic eddies," in *Ocean modeling in an eddying regime* (Washington, D. C., USA: American Geophysical Union (AGU), 5–15. doi: 10.1029/177GM03

McWilliams, J. C. (2016). Submesoscale currents in the ocean. *Proc. R. Soc. A: Math. Phys. Eng. Sci.* 472, 20160117–20160117. doi: 10.1098/rspa.2016.0117

Millard, R. C., Owens, W. B., and Fofonoff, N. P. (1990). On the calculation of the Brunt-Väisälä frequency. *Deep Sea Res. Part A Oceanogr. Res. Papers* 37, 167–181. doi: 10.1016/0198-0149(90)90035-T

Mizobata, K., Saitoh, S. I., Shiomoto, A., Miyamura, T., Shiga, N., Imai, K., et al. (2002). Bering Sea cyclonic and anticyclonic eddies observed during summer 2000 and 2001. *Prog. Oceanogr.* 55, 65–75. doi: 10.1016/S0079-6611(02)00070-8

Murphy, K. R., Butler, K. D., Spencer, R. G. M., Stedmon, C. A., Boehme, J. R., and Aiken, G. R. (2010). Measurement of dissolved organic matter fluorescence in aquatic environments: an interlaboratory comparison. *Environ. Sci. Technol.* 44, 9405–9412. doi: 10.1021/es102362t

Nagai, T., Tandon, A., Gruber, N., and McWilliams, J. C. (2008). Biological and physical impacts of ageostrophic frontal circulations driven by confluent flow and vertical mixing. *Dyn. Atmos. Oceans*45, 229–251. doi: 10.1016/j.dynatmoce.2007.12.001

Nelson, N. B., Carlson, C. A., and Steinberg, D. K. (2004). Production of chromophoric dissolved organic matter by Sargasso Sea microbes. *Mar. Chem.* 89, 273–287. doi: 10.1016/j.marchem.2004.02.017

Nelson, N. B., and Siegel, D. A. (2013). The global distribution and dynamics of chromophoric dissolved organic matter. *Annu. Rev. Mar. Sci.* 5, 447–476. doi: 10.1146/annurev-marine-120710-100751

Nieto-Cid, M., Álvarez-Salgado, X. A., and Pérez, F. F. (2006). Microbial and photochemical reactivity of fluorescent dissolved organic matter in a coastal upwelling system. *Limnol. Oceanogr.* 51, 1391–1400. doi: 10.4319/lo.2006.51.3.1391

Noyon, M., Morris, T., Walker, D., and Huggett, J. (2019). Plankton distribution within a young cyclonic eddy off south-western Madagascar. *Deep Sea Res. Part II: Topical Stud. Oceanogr.* 166, 141–150. doi: 10.1016/j.dsr2.2018.11.001

Omori, Y., Saeki, A., Wada, S., Inagaki, Y., and Hama, T. (2020). Experimental analysis of diurnal variations in humic-like fluorescent dissolved organic matter in surface seawater. *Front. Mar. Sci.* 7. doi: 10.3389/fmars.2020.589064

Pastor, M. V., Vélez-Belchí, P., and Hernández-Guerra, A. (2015). "Water masses in the Canary Current Large Marine Ecosystem," in *Oceanographic and biological features in the Canary Current Large Marine Ecosystem*. Eds. L. Valdés and I. Déniz-GonzálezIOC Technical Series, No. 115 (IOC-UNESCO, Paris), 73–79. Available online at: http://hdl.handle.net/1834/9178 (Accessed Feburuary 9, 2026).

Pérez, F. F., Ríos, A. F., King, B. A., and Pollard, R. T. (1995). Decadal changes of the θ–S relationship of the Eastern North Atlantic Central Water. *Deep Sea Res. Part I: Oceanogr. Res. Papers* 42, 1849–1864. doi: 10.1016/0967-0637(95)00091-7

Riley, J. S., Sanders, R., Marsay, C., Le Moigne, F. A. C., Achterberg, E. P., and Poulton, A. J. (2012). The relative contribution of fast and slow sinking particles to ocean carbon export. *Global Biogeochem. Cycles* 26, GB1026. doi: 10.1029/2011GB004085

Sangrà, P., Pelegrí, J. L., Hernández-Guerra, A., Arregui, I., Martín, J. M., and Marrero-Díaz, A. (2005). Life history of an anticyclonic eddy. *J. Geophys. Res.: Oceans* 110. doi: 10.1029/2004JC002526

Sangrà, P., Auladell, M., Marrero-Díaz, A., Pelegrí, J. L., Fraile-Nuez, E., Rodríguez-Santana, A., et al. (2007). On the nature of oceanic eddies shed by the Island of Gran Canaria. *Deep Sea Res. Part I: Oceanogr. Res. Papers* 54, 687–709. doi: 10.1016/j.dsr.2007.02.004

Sangrà, P., Pascual, A., Rodríguez-Santana, Á., Machín, F., Mason, E., McWilliams, J. C., et al. (2009). The Canary Eddy Corridor: A major pathway for long-lived eddies in the subtropical North Atlantic. *Deep Sea Res. Part I: Oceanogr. Res. Papers* 56, 2100–2114. doi: 10.1016/j.dsr.2009.08.008

Santana-Falcón, Y., Álvarez-Salgado, X. A., Pérez-Hernández, M. D., Hernández-Guerra, A., Mason, E., and Arístegui, J. (2017). Organic carbon budget for the eastern boundary of the North Atlantic subtropical gyre: major role of DOC in mesopelagic respiration. *Sci. Rep.* 7, 10129–10129. doi: 10.1038/s41598-017-10974-y

Shi, W., Lin, H., Deng, Q., and Hu, J. (2024). Asymmetry of submesoscale instabilities in anticyclonic and cyclonic eddies. *Geophys. Res. Lett.* 51, e2023GL106853–e2023GL106853. doi: 10.1029/2023GL106853

Stedmon, C. A., and Nelson, N. B. (2015). "Chapter 10 - the optical properties of DOM in the ocean," in *Biogeochemistry of marine dissolved organic matter, 2nd ed.* Eds. D. A. Hansell and C. A. Carlson (Academic Press, Boston), 481–508. doi: 10.1016/B978-0-12-405940-5.00010-8

Sweeney, E. N., McGillicuddy, D. J., and Buesseler, K. O. (2003). Biogeochemical impacts due to mesoscale eddy activity in the Sargasso Sea as measured at the Bermuda Atlantic Time-series Study (BATS). *Deep Sea Res. Part II: Topical Stud. Oceanogr.* 50, 3017–3039. doi: 10.1016/j.dsr2.2003.07.008

Valencia, L. P., Rodríguez-Santana, Á., Aguiar-Gonzaléz, B., Arístegui, J., Álvarez-Salgado, X. A., Coca, J., et al. (2025). Mesoscale dynamics of an intrathermocline eddy in the Canary Eddy Corridor. *EGUsphere* 2025, 1–46. doi: 10.5194/egusphere-2025-99

Wang, C., Guo, W., Li, Y., Stubbins, A., Li, Y., Song, G., et al. (2017). Hydrological and biogeochemical controls on absorption and fluorescence of dissolved organic matter in the northern south China sea. *J. Geophys. Res.: Biogeosci.* 122, 3405–3418. doi: 10.1002/2017JG004100

Weishaar, J. L., Aiken, G. R., Bergamaschi, B. A., Fram, M. S., Fujii, R., and Mopper, K. (2003). Evaluation of specific ultraviolet absorbance as an indicator of the chemical composition and reactivity of dissolved organic carbon. *Environ. Sci. Technol.* 37, 4702–4708. doi: 10.1021/es030360x

Winkler, L. W. (1888). Die Bestimmung des im Wasser gelösten Sauerstoffes. *Berichte der Dtsch. Chem. Ges.* 21, 2843–2854. doi: 10.1002/cber.188802102122

Xiao, X., Yamashita, Y., Gonsior, M., and Jiao, N. (2023). The efficiency of the microbial carbon pump as seen from the relationship between apparent oxygen utilization and

fluorescent dissolved organic matter. *Prog. Oceanogr.* 210, 102929–102929. doi: 10.1016/j.pocean.2022.102929

Yamashita, Y., and Tanoue, E. (2003). Chemical characterization of protein-like fluorophores in DOM in relation to aromatic amino acids. *Mar. Chem.* 82, 255–271. doi: 10.1016/S0304-4203(03)00073-2

Zhang, Z., Qiu, B., Klein, P., and Travis, S. (2019). The influence of geostrophic strain on oceanic ageostrophic motion and surface chlorophyll. *Nat. Commun.* 10, 2838–2838. doi: 10.1038/s41467-019-10883-w

Zhou, K., Dai, M., Xiu, P., Wang, L., Hu, J., and Benitez-Nelson, C. R. (2020). Transient enhancement and decoupling of carbon and opal export in cyclonic eddies. *J. Geophys. Res.: Oceans* 125, e2020JC016372–e2020JC016372. doi: 10.1029/2020JC016372

Zhu, X.-Y., Yang, Z., Xie, Y., Zhou, K., and Wang, W.-L. (2023). Strong particle dynamics counteract the nutrient-pumping effect leading to weak carbon flux in a cyclonic eddy. *Mar. Chem.* 255, 104279–104279. doi: 10.1016/j.marchem.2023.104279